

1 **New fire diurnal cycle characterizations to improve fire radiative**  
2 **energy assessments made from MODIS observations**

3  
4 N. Andela<sup>1</sup>, J. W. Kaiser<sup>2</sup>, G. R. van der Werf<sup>1</sup>, and M. J. Wooster<sup>3,4</sup>

5  
6 <sup>1</sup>Faculty of Earth and Life Sciences, VU University, Amsterdam, the Netherlands

7 <sup>2</sup>Max-Planck-Institut für Chemie, Mainz, Germany

8 <sup>3</sup>Kings College London, Environmental Monitoring and Modelling Research Group, Department of  
9 Geography, London WC2R 2LS, UK

10 <sup>4</sup>NERC National Centre for Earth Observation (NCEO), UK

11  
12 Received: 2 January 2015 – Accepted: 10 March 2015 – Published: 31 March 2015

13  
14 Correspondence to: N. Andela (niels.andela@nasa.gov)

15

16 **Abstract**

17

18 Accurate near real time fire emissions estimates are required for air quality forecasts. To date, most  
19 approaches are based on satellite-derived estimates of fire radiative power (FRP), which can be  
20 converted to fire radiative energy (FRE) which is directly related to fire emissions. Uncertainties in  
21 these FRE estimations are often substantial. This is for a large part because the most often used low-  
22 Earth orbit satellite-based instruments such as the MODerate-resolution Imaging Spectroradiometer  
23 (MODIS) have a relatively poor sampling of the usually pronounced fire diurnal cycle. In this paper we  
24 explore the spatial variation of this fire diurnal cycle and its drivers using data from the geostationary  
25 Meteosat Spinning Enhanced Visible and Infrared Imager (SEVIRI). In addition, we sampled data from  
26 the SEVIRI instrument at MODIS detection opportunities to develop two approaches to estimate  
27 hourly FRE based on MODIS active fire detections. The first approach ignored the fire diurnal cycle,  
28 assuming persistent fire activity between two MODIS observations, while the second approach  
29 combined knowledge on the climatology of the fire diurnal cycle with active fire detections to  
30 estimate hourly FRE. The full SEVIRI time-series, providing full coverage of the fire diurnal cycle, were  
31 used to evaluate the results. Our study period comprised of three years (2010–2012), and we  
32 focussed on Africa and the Mediterranean basin to avoid the use of potentially lower quality SEVIRI  
33 data obtained at very far off-nadir view angles. We found that the fire diurnal cycle varies  
34 substantially over the study region, and depends on both fuel and weather conditions. For example,  
35 more “intense” fires characterized by a fire diurnal cycle with high peak fire activity, long duration  
36 over the day, and with nighttime fire activity are most common in areas of large fire size (i.e., large  
37 burned area per fire event). These areas are most prevalent in relatively arid regions. Ignoring the  
38 fire diurnal cycle generally resulted in an overestimation of FRE, while including information on the  
39 climatology of the fire diurnal cycle improved FRE estimates. The approach based on knowledge of  
40 the climatology of the fire diurnal cycle also improved distribution of FRE over the day, although only  
41 when aggregating model results to coarser spatial and/or temporal scale good correlation was found  
42 with the full SEVIRI hourly reference dataset. We recommend the use of regionally varying fire  
43 diurnal cycle information within the Global Fire Assimilation System (GFAS) used in the Copernicus  
44 Atmosphere Monitoring Services, which will improve FRE estimates and may allow for further  
45 reconciliation of biomass burning emission estimates from different inventories.

46

## 47 **1 Introduction**

48

49 Landscape fires are a global phenomena, and the annually burned area is roughly equivalent to the  
50 area of India (Giglio et al., 2013). Most burned area occurs in the savannas of Africa, Australia, and  
51 South America, where they shape ecosystem dynamics and due to their scale are an important  
52 source of global emissions of (greenhouse) gases and aerosols (Seiler and Crutzen, 1980; Bowman et  
53 al., 2009). Fires affect air quality both locally and regionally (Langmann et al., 2009), with recent  
54 studies putting mortality rates over 300000 annually due to exposure to smoke (Johnston et al.,  
55 2012).

56

57 Traditionally, the amount of dry matter burned and quantity of trace gases and aerosols emitted  
58 have been calculated using biome-specific fire return intervals and estimates of the total amount of  
59 biomass as well as the fraction of biomass burned, the combustion completeness (Seiler and Crutzen,  
60 1980). Thanks to new satellite input streams that better capture the spatial and temporal diffuse  
61 nature of fires, the estimated fire return intervals have been replaced by direct estimates of monthly,  
62 weekly or even daily area burned (Roy et al., 2005; Giglio et al., 2009). In addition, satellite  
63 information and biogeochemical modelling have been used to improve estimates of biomass and  
64 combustion completeness. However, uncertainties in these bottom-up fire emission estimates are  
65 still substantial (Reid et al., 2009; Zhang et al., 2012; Larkin et al., 2014), and they are generally  
66 inappropriate for use in near real-time systems partly because the burned area signature is only  
67 detectable days to weeks after the actual fire occurrence.

68

69 Hot spot observations from satellite have been used as a proxy for burned area and emissions fluxes  
70 in near real time (Freitas et al., 2005; Reid et al., 2009; Wiedinmyer et al., 2011). Another promising  
71 and relatively new bottom up approach uses estimates of fire radiative power (FRP) observed from  
72 satellite to calculate daily fire radiative energy (FRE). Wooster et al. (2005) found that these FRE  
73 estimates scale directly to dry matter burned, potentially circumventing the uncertainties associated  
74 with estimating area burned, fuel loads, and the combustion completeness. In addition, FRP  
75 observations can be observed and processed in near real time (Xu et al., 2010; Kaiser et al., 2012;  
76 Zhang et al., 2012) and can be measured for small fires that remain undetected in burned area  
77 products (Roberts et al., 2011; Randerson et al., 2012).

78

79 Hot spot and FRP observations are currently the only available options when modelling exercises  
80 require near real time observations, for example in chemical weather forecasts used to predict air  
81 quality. The Global Fire Assimilation System (GFAS; Kaiser et al., 2012), for example, is used to  
82 estimate global near real time daily fire emissions within the EU-funded project Monitoring  
83 Atmospheric Composition and Climate III (MACC-III). GFAS is currently using fire observations from  
84 the polar orbiting MODERate-resolution Imaging Spectroradiometer (MODIS) instruments aboard the  
85 Terra and Aqua satellites (Giglio et al., 2006). Due to their relative proximity to the Earth, the Terra  
86 and Aqua MODIS instruments have a high sensitivity to even quite low FRP (smaller and/or lower  
87 intensity) fires. However, they only provide four daily observations under ideal conditions but less  
88 when optically thick clouds are present, which may not be enough to fully characterize how fire  
89 activity varies over the course of the day. Observations with a much higher temporal resolution are  
90 available from geostationary satellites. However, as a consequence of their geostationary position,

91 these satellites individually do not provide global data and are located at greater distance from the  
92 Earth resulting in typically coarser pixel sizes than polar orbiting instruments. Since the threshold of  
93 detectability of a fire is not only dependent on the instrument but also a function of the pixel area,  
94 geostationary sensors have a higher minimum FRP detection limit (typically > 40 MW) than MODIS (~  
95 8 MW). They therefore do not observe the lowest FRP component of the fire regime (Roberts et al.,  
96 2005; Freeborn et al., 2014).

97  
98 Previous studies found that fire activity shows a strong diurnal cycle, and one that is both temporally  
99 and spatially variable (Prins and Menzel, 1992; Giglio, 2007; Roberts et al., 2009). The ideal set-up to  
100 detect fires would be a high temporal resolution imaging system, sensitive to even the lowest FRP  
101 fires, and providing global coverage, but due to the limitations of the orbital characteristics outlined  
102 above there is no single platform available to provide this. Therefore the estimation of FRE at a global  
103 scale is difficult, with polar orbiting satellites lacking observations to accurately represent the fire  
104 diurnal cycle and geostationary satellites being limited to certain regions of the globe and omitting  
105 the (rather common) low FRP fires. However, previous studies have developed approaches to  
106 estimate FRE based on the combination of data from different satellite systems (Boschetti and Roy,  
107 2009; Ellicott et al., 2009; Freeborn et al., 2009, 2011; Vermote et al., 2009).

108  
109 Some of these mixed approaches used both burned area and active fire data (Boschetti and Roy,  
110 2009; Roberts et al., 2011), which may provide benefits in terms of more accurate FRE determination  
111 but cannot be used easily in near real time systems because of the latency in burned area  
112 observations. Alternatively, FRP observations of polar orbiting and geostationary satellites can be  
113 blended to combine the sensitivity of the MODIS instruments to lower FRP fires and the diurnal  
114 sampling characteristics of SEVIRI. Freeborn et al. (2009) developed a database for matching SEVIRI  
115 and MODIS FRP observations based on frequency-magnitude statistics, but the samples had to be  
116 accumulated over significant spatial areas (5°) to provide matchable statistics, which is incompatible  
117 with the need to develop a method operating at high spatial resolution. Freeborn et al. (2011) later  
118 presented an alternative approach, estimating FRE using MODIS data accumulated over 8 day  
119 periods over which MODIS samples a location at the fullest range of view zenith angles. The  
120 relationship between the “true” FRE and the limited number of FRP samples provided by MODIS was  
121 derived using SEVIRI FRP time-series sampled at the MODIS sampling interval. Vermote et al. (2009)  
122 and Ellicott et al. (2009) used a different approach to create FRE data from MODIS, showing that for  
123 several regions of the globe the fire diurnal cycle can be described by a Gaussian function, and used  
124 monthly MODIS data to fit the parameters of the Gaussian. Using this approach, a first global  
125 estimation of monthly FRE was made (Ellicott et al., 2009). Despite the success of these latter  
126 approaches with regard to estimating FRE from MODIS, they are not a solution to the problem posed  
127 herein because they require 8 days of consecutive MODIS data and therefore cannot be applied in a  
128 near real-time approach.

129  
130 Global fire emissions estimates at high spatial and temporal resolutions, ideally produced in near real  
131 time, are required to feed into atmospheric models which are under continuous development and  
132 run at improved resolutions thanks to increased computational power (Zhang et al., 2012). Higher  
133 temporal resolution may also help to reconcile bottom up and top down emission estimates (Mu et  
134 al., 2011). None of the approaches mentioned above are, however, suitable for providing this. Due to  
135 these limitations current state of the art global near real time emission inventories still ignore

136 possible effects of fire diurnal cycle on their emission estimates (e.g., Wiedinmyer et al., 2011; Kaiser  
137 et al., 2012) and may therefore be structurally biased due to the fire diurnal cycle and the MODIS  
138 sampling design (e.g., Ichoku et al., 2008; Ellicott et al., 2009; Freeborn et al., 2011).

139

140 The purpose of the work presented here is to better understand the fire diurnal cycle and its  
141 spatiotemporal dynamics, in order to develop a new way to include this into a near real time fire  
142 emissions estimation framework. First, the spatial distribution and dependencies of the fire diurnal  
143 cycle and their effect on active fire detections at MODIS overpasses were explored. Then, data  
144 assimilation was used to compare two different methods to derive hourly FRE estimates at 0.1°  
145 resolution based on low Earth-orbiting MODIS observations. The first method ignored the fire diurnal  
146 cycle, and was used as a reference to better understand the combined effect of the fire diurnal cycle  
147 and the MODIS sampling design on hourly FRE estimates. The second method combined knowledge  
148 on the fire diurnal cycle with active fire detections at MODIS overpasses. Following previous studies  
149 (Freeborn et al., 2009, 2011), we used FRP observations derived from data collected by the  
150 geostationary SEVIRI instrument at MODIS detection opportunities, rather than actual MODIS  
151 observations, to drive the two model approaches and we evaluated the model results against the full  
152 SEVIRI time-series. We used three years of active fire data (2010–2012) across Africa and the  
153 Mediterranean basin to include a wide range of climates and land cover types, and avoid the use of  
154 SEVIRI observations obtained at very far off-nadir angles over South America and northern Europe  
155 (Freeborn et al., 2014). Results are intended for application in GFAS within EU’s Copernicus  
156 Atmosphere Monitoring Service (CAMS, <http://atmosphere.copernicus.eu>).

157

## 158 **2 Data**

159

160 To explore the spatiotemporal dynamics of the fire diurnal cycle, we used hourly temporal resolution  
161 FRP data derived from 15 min observations made by the SEVIRI instrument hosted onboard the  
162 geostationary Meteosat satellite (Sect. 2.1). However, to drive the models developed here we only  
163 used SEVIRI FRP observations made at the overpass times of the MODIS polar orbiting sensors (Sect.  
164 2.2), whilst the hourly temporal resolution SEVIRI time-series were used to evaluate the results. Land  
165 cover characteristics (Sect. 2.3), along with data on fire size (Sect. 2.4), were used to better  
166 understand the spatial distribution of fire diurnal cycle. These datasets are described in more detail  
167 below, followed by the methods used in Sect. 3.

168

### 169 ***2.1 SEVIRI fire radiative power (FRP)***

170

171 The SEVIRI instrument aboard the geostationary Meteosat Second Generation (MSG) series of  
172 satellites provides coverage of the full Earth disk every 15 min in 12 spectral bands (Schmetz et al.,  
173 2002). The Meteosat SEVIRI FRP-PIXEL product contains per-pixel fire radiative power data along with  
174 FRP uncertainty metrics produced from the full spatial and temporal resolution SEVIRI observations  
175 (Wooster et al., 2015). The FRP-PIXEL product is produced using an operational version of the  
176 geostationary Fire Thermal Anomaly (FTA) algorithm described in Roberts and Wooster (2008), and  
177 the product and its performance characteristics are described in Wooster et al. (2015). The FRP-PIXEL

178 products are freely available from the Land Surface Analysis Satellite Applications Facility (LSASAF;  
179 <http://landsaf.meteo.pt>), from the EUMETSAT EO Portal (<https://eoportal.eumetsat.int>) or via the  
180 EUMETCAST dissemination service (<http://www.eumetsat.int>) in both real-time and archived form,  
181 as detailed in Wooster et al. (2015). The Meteosat satellites are located at 0° longitude and latitude,  
182 and at nadir the SEVIRI pixels cover 3 km x 3 km on the ground, but this degrades with increasing  
183 view angle away from the West African sub-satellite point (Freeborn et al., 2011; Roberts et al.,  
184 2015). The FRP-PIXEL product data used here were obtained from the LSA SAF and were rescaled to  
185 an hourly 0.1° resolution with the GFAS gridding algorithm explained in Kaiser et al. (2012). Missing  
186 FRP values in individual observations within the hour (e.g., due to smoke or short periods of cloud  
187 cover) were thus implicitly ignored. A single 0.1° grid cell comprises over 13 SEVIRI pixels close to the  
188 sub-satellite point (equatorial West Africa) and this reduces to around 6 SEVIRI pixels at greater of  
189 nadir angles (e.g., Portugal and Madagascar). Data were archived in the Meteorological Archival and  
190 Retrieval System (MARS) of the European Centre for Medium range Weather Forecasting (ECMWF)  
191 prior to their use herein.

192

## 193 **2.2 MODIS detection opportunity**

194

195 The two MODIS sensors on board of the Terra and Aqua satellites provide 4 daily overpasses in most  
196 Earth locations, albeit sometimes at view angles in excess of 45° where the product performance is  
197 somewhat degraded (Freeborn et al., 2011). At nadir the MODIS thermal channel spatial resolution is  
198 1 km, but decreases away from the swath centre (Freeborn et al., 2011). We used the MODIS MOD03  
199 (Terra) and MYD03 (Aqua) geolocation products to determine where and when MODIS data were  
200 collected within the SEVIRI Earth disk. As cloud cover may further limit the fire detection opportunity,  
201 we used the data quality and cloud cover information of the MOD14 and MYD14 active fire products  
202 to filter out grid cells with cloud cover (Giglio et al., 2006). Here we define the detection opportunity  
203 as the ability to make unobstructed observations, and the MODIS detection opportunity was derived  
204 by combining the MOD03, MYD03, MOD14 and MYD14 products, combining overpass times and  
205 cloud cover. We used MODIS data from Collection 5. Like the SEVIRI data, these data were rescaled  
206 to hourly 0.1° resolution with the GFAS gridding algorithm and archived in MARS (Kaiser et al., 2012).  
207 The data were archived for the Terra and Aqua satellites separately. The original MODIS swath data  
208 can be downloaded from NASA at <http://reverb.echo.nasa.gov>.

209

## 210 **2.3 MODIS Land cover**

211

212 The dominant land cover type was derived from the MODIS MCD12C1 land cover product, which  
213 provides 0.05° spatial resolution annual information on land cover (Friedl et al., 2002). We calculated  
214 the dominant land cover type for each grid cell as the land cover type that on average covered the  
215 largest fraction during the study period (2010–2012). The University of Maryland (UMD) classification  
216 scheme was used, and data was rescaled to 0.1° resolution. Because we only considered Africa and  
217 the Mediterranean basin in this study, and because in some land cover classes very few fires  
218 occurred, we could merge some land cover classes that were of relatively little importance for our  
219 study. Specifically, all forest classes within the tropics were binned into the tropical forest class, while

220 extratropical forests were all labelled temperate forest. Open and closed shrublands were merged  
221 into one shrubland class, and urban and built-up, barren or sparsely vegetated into grasslands.  
222

## 223 **2.4 Fire size**

224  
225 Here we define the fire size for a certain grid cell as the mean burned area per fire event, weighted  
226 by their total area burnt (when calculating the mean, a fire event burning 100 km<sup>2</sup> is assigned one  
227 hundred times the weight of an event burning 1 km<sup>2</sup>). The MODIS MCD64A1 burned area product  
228 provides daily mapped estimates of global burned area (Giglio et al., 2009). We applied the methods  
229 described by Archibald and Roy (2009) to derive a global mean fire “size” (area) map using data over  
230 our study period (2010–2012). We made one modification to the approach described by Archibald  
231 and Roy (2009): we assumed that two neighbouring burned area grid cells only belonged to the same  
232 fire if the burn date was no longer than two days apart (instead of 8 days). We believe that overall  
233 this provides a better estimation of the fire size in our study region, as the vast majority of fires here  
234 are grass fires, occurring outside tropical forest zones and thus spreading relatively fast while being  
235 relatively less often obstructed by cloud cover. Consequently, the uncertainty in burn date is  
236 generally low in our study region (Giglio et al., 2013) and so the two day thresholds was deemed  
237 more appropriate.  
238

## 239 **3 Methods**

240  
241 Our overall goal within GFAS is to provide hourly estimates of FRE at 0.1° spatial resolution, based on  
242 the limited number of MODIS overpasses available each day at each grid cell location. This limited  
243 number of daily MODIS observations, in combination with the often pronounced fire diurnal cycle,  
244 are the major obstacles in providing the required output. We first studied the spatiotemporal  
245 variation of the fire diurnal cycle, in an attempt to understand its variability (Sect. 3.1). Then, we  
246 explored the way the fire diurnal cycle affects active fire detections made at the MODIS sampling  
247 times (Sect. 3.2). Using this knowledge we explored a new method to parameterize the fire diurnal  
248 cycle, and compared results to a modelling approach in which the fire diurnal cycle is ignored.  
249 Building on the work of Freeborn et al. (2009, 2011), to drive the modelling approaches we used  
250 SEVIRI data sampled at the MODIS detection opportunities (according to the hourly data  
251 representation introduced above), rather than actual MODIS observations (Sect. 3.2). This allowed us  
252 to focus on the issue of diurnal cycle sampling rather than simultaneously dealing with the issue of  
253 MODIS and SEVIRI’s differential sensitivity to active fires (Freeborn et al., 2009).  
254

255 Using data assimilation we combined the discrete actual SEVIRI observations, made at the time of the  
256 MODIS detection opportunities, with hourly predictions of fire activity – using their combination to  
257 create continuous hourly best estimate FRE time-series (Sect. 3.3). We developed two prediction  
258 methods. The first method assumed persistent fire activity until the next satellite detection  
259 opportunity, and provides further insights into the combined effect of the fire diurnal cycle and the  
260 MODIS sampling design on hourly FRE estimates when the fire diurnal cycle is ignored (Sect. 3.4). The  
261 second method followed previous studies and used a Gaussian function to predict fire development

262 over the day (Vermote et al., 2009). By combining prior knowledge about the climatology of the fire  
 263 diurnal cycle with active fire observations at MODIS overpasses to estimate the parameters of the  
 264 Gaussian function, this approach provides a possible pathway to implement the fire diurnal cycle into  
 265 the near real time fire emission modelling framework (Sect. 3.5). Comparing the results of the two  
 266 approaches to those from the full hourly SEVIRI time-series allowed us to determine and discuss their  
 267 strengths and limitations (Sect. 3.6).

### 269 **3.1 Exploring the fire diurnal cycle**

270  
 271 We started exploring the fire diurnal cycle and its drivers. A Gaussian function was optimally fitted  
 272 (least squares) to the hourly SEVIRI observations  $\tilde{\rho}_{SEV(t)}$  for each grid cell and day of fire activity  
 273 during the study period:

$$274 \quad \tilde{\rho}_{SEV(t)} = \rho_{base} + (\rho_{peak} - \rho_{base})e^{-\frac{(h_t - h_{peak})^2}{2\sigma^2}}. \quad (1)$$

275  
 276 Where  $\rho_{base}$  corresponds to the nighttime fire activity,  $\rho_{peak}$  to the maximum FRP for a given day,  $\sigma$   
 277 is the standard deviation (SD) of FRE distribution over the day (dependent on fire duration),  $h_t$  is the  
 278 local solar time at time step  $t$  and  $h_{peak}$  is the local hour at which FRP reaches its daily maximum.  
 279 This resulted in a database containing hourly time-series of  $\tilde{\rho}_{SEV(t)}$  and the fitted Gaussian function,  
 280 and daily time-series of optimal parameter values of the Gaussian function for each grid cell. At the  
 281 same time we also kept track of hourly MODIS detection opportunities. This enabled us get a better  
 282 understanding of structural errors caused by the MODIS sampling design in relation to the actual fire  
 283 diurnal cycle.

284  
 285 Although the fire diurnal cycle as observed by SEVIRI is comparable to that which would be observed  
 286 by MODIS if it had the same temporal sampling ability, it is a little different due to SEVIRI's inability to  
 287 discriminate the lowest FRP fire pixels which typically dominate more towards the start and end of  
 288 the daily fire cycle, but which are also present along with often higher FRP pixels towards the diurnal  
 289 cycle maxima (Freeborn et al., 2009). To gauge the magnitude of the effect Freeborn et al. (2009)  
 290 derived the "virtual MODIS" fire product that has the temporal sampling of SEVIRI and the sensitivity  
 291 to fire of MODIS. They found that the full-width at half maximum height (i.e., the width of the diurnal  
 292 cycle at half of the daily FRP maximum value) of the diurnal cycles derived from the SEVIRI and the  
 293 "virtual MODIS" datasets are very similar, it is the amplitude and the full-width at base height of the  
 294 two cycles, which are more different. In terms of total FRE emitted, the latter is of less importance,  
 295 here we followed Freeborn et al. (2011) in assuming that the diurnal cycles from SEVIRI and MODIS  
 296 are sufficiently similar.

297  
 298 In order to visualize the spatial distribution of the fire diurnal cycle, the climatological diurnal cycle  
 299 was calculated for each grid cell depending on the mean parameter values of the Gaussian function  
 300 weighted for daily FRE, including all days of fire activity during the study period without cloud  
 301 obscurance. To get a better understanding of the drivers of the fire diurnal cycle these results were

302 compared to land cover and aspects of the fire regime (fire size, total annual FRE, and the annual  
303 number of days with fire activity), see Sect. 2.  
304

### 305 **3.2 Sampling SEVIRI data at MODIS detection opportunities**

306  
307 During the data assimilation, SEVIRI observations at MODIS detection opportunities were used to  
308 drive the models. Here, SEVIRI observations for a given hour  $t$  are given by  $\tilde{\rho}_{SEV(t)}$  and SEVIRI fraction  
309 of observed area by  $\tilde{\alpha}_{SEV(t)}$ ; in the same way, observations of the MODIS instruments are given by  
310  $\tilde{\rho}_{MOD(t)}$  and  $\tilde{\alpha}_{MOD(t)}$ . Therefore input for the models, i.e., the SEVIRI observations at MODIS  
311 detection opportunity times ( $\tilde{\rho}_t$  and  $\tilde{\alpha}_t$ ) for a given hour  $t$  are given by:  
312

$$\tilde{\rho}_t = \tilde{\rho}_{SEV(t)} \quad (2)$$

$$\tilde{\alpha}_t = \tilde{\alpha}_{MOD(t)}. \quad (3)$$

313  
314 For clarity, we assumed that the observed FRP  $\tilde{\rho}_t$  is zero when there was no MODIS detection  
315 opportunity. Anyhow, during the data assimilation  $\tilde{\rho}_t$  was weighted for observed area  $\tilde{\alpha}_t$ , which was  
316 zero when there was no observation.

317  
318 SEVIRI data sampled at MODIS detection opportunities were compared to the full SEVIRI hourly time-  
319 series to explore the effect of the fire diurnal cycle on the daily sampling at MODIS overpasses. More  
320 specifically we calculated the percentage of FRE emitted on days without any active fire detection at  
321 MODIS detection opportunities, and the total daily number of MODIS overpasses during the fire  
322 season. The latter was calculated by weighing the mean number of monthly detection opportunities  
323 at MODIS overpasses by monthly total detected FRP, thus giving the largest weight to the month with  
324 most fire activity (ignoring cloud cover).  
325

### 326 **3.3 Data assimilation**

327  
328 We used a modified version the fire data assimilation methodology of GFAS to allow representation  
329 of the fire diurnal cycle. GFAS assumes that the availability of observations dominates the error  
330 budget of the global FRP fields. It approximates these errors by further assuming the FRP variance to  
331 be inversely proportional to the fraction of observed area  $\tilde{\alpha}_t$ . Thus the variance increases with  
332 decreasing partial cloud cover and with the number of satellite observations. In the following data  
333 assimilation, GFAS fills observation gaps with a Kalman filter, in which current observations are  
334 combined with information from earlier ones. The Kalman filter has a time step of 1 day. It uses a  
335 trivial predictive model for the temporal evolution of FRP (i.e., persistence), and assumes for the  
336 accuracy of the 1 day FRP prediction that the variance increases by a factor of 9 (Kaiser et al., 2012).  
337

338 Our modifications affected the step size and the FRP prediction model. The former was set to 1h to  
339 be able to represent a diurnal cycle. For calculating the FRP prediction  $\check{\rho}_t$ , we investigated two  
340 different approaches (Sects. 3.4 and 3.5). In both cases, we assumed for the accuracy of the 1h FRP  
341 prediction that the variance increases by a factor of 4. Lowering the value compared to the daily

342 GFAS is motivated by the shorter time step used in our study. However, lowering it too much would  
 343 not give sufficient weight to new FRP observations. Thus the analysis FRP  $\hat{\rho}_t$  and “fraction of  
 344 observed area”  $\hat{\alpha}_t$  were calculated at each 1h time step by optimal interpolation as follows, cf. Eqs.  
 345 (32)–(33) of Kaiser et al. (2012):

$$\hat{\rho}_t = \frac{1}{\hat{\alpha}_t} \left( \frac{\hat{\alpha}_{t-1}}{5} \check{\rho}_t + \tilde{\alpha}_t \tilde{\rho}_t \right) \quad (4)$$

347  
 348 with  $\check{\rho}_t$  according to Sects. 3.4 and 3.5 and

$$\hat{\alpha}_t = \frac{\hat{\alpha}_{t-1}}{5} + \tilde{\alpha}_t. \quad (5)$$

349

### 350 **3.4 Persistent approach**

351

352 Applying the daily persistence approach of Kaiser et al. (2012) to hourly time resolution, we first  
 353 explored the most parsimonious approach that predicts FRP  $\check{\rho}_t$  as being equal to the FRP of the  
 354 previous time step’s analysis:

355

$$\check{\rho}_t = \hat{\rho}_{t-1}. \quad (6)$$

356

357 This approach provided insights in the spatiotemporal consequences for FRE estimation when  
 358 information on the fire diurnal cycle is not incorporated.

359

### 360 **3.5 Climatological approach**

361

362 In the second approach we followed previous studies of Vermote et al. (2009) and Ellicot et al. (2009)  
 363 and the recommendation in Kaiser et al. (2009) to use a Gaussian function to describe a “standard  
 364 fire diurnal cycle”. Wooster et al. (2005) and Roberts et al. (2009) already demonstrated that SEVIRI  
 365 observations sample the diurnal cycle of large fires well, and for some individual large fires show FRP  
 366 time-series that depict diurnal characteristics appearing close to Gaussian in nature even at 15 min  
 367 temporal resolution. The prediction was calculated by optimally fitting a Gaussian function through  
 368 the last 24h of analysis:

369

$$\check{\rho}_t = \rho_{base} + (\rho_{peak} - \rho_{base}) e^{-\frac{(h_t - h_{peak})^2}{2\sigma^2}} \quad (7)$$

370

371 However, only  $h_{peak}$  was optimally fitted, by minimizing the sum of least squares between the  
 372 Gaussian function and the previous 24h of the analysis:

373

$$\hat{\rho}_{t-24}, \hat{\rho}_{t-23}, \dots, \hat{\rho}_{t-1}. \quad (8)$$

374

375 Following previous studies that found that fire diurnal cycle is land cover dependent (Giglio, 2007;  
376 Roberts et al., 2009; Vermote et al., 2009; Freeborn et al., 2011), we used land cover (LC) average  
377 values  $\sigma_{LC}$  for  $\sigma$  (weighted by FRE). Values of  $\rho_{base}$  and  $\rho_{peak}$  on the other hand could be directly  
378 related to daily MODIS observations. We followed Vermote et al. (2009) to use the mean of the  
379 nighttime (defined here as 6p.m.–6a.m. the next day) observations at MODIS detection opportunities  
380 to determine  $\rho_{base}$ . To relate SEVIRI observations at MODIS detection opportunities to  $\rho_{peak}$  the ratio  
381 of mean daytime (6a.m.–6p.m.) FRP observations at MODIS detection opportunities to mean  $\rho_{peak}$   
382 was calculated per land cover type. We used per land cover average values for scaling the daytime  
383 observations at MODIS detection opportunities to  $\rho_{peak}$  rather than the values found per grid cell to  
384 keep the model generic and globally applicable. Finally, if there were no active fires observed during  
385 the previous 24h, we forced the prediction to be zero, to prevent fires from continuing during long  
386 periods of no observations.  
387

### 388 **3.6 Model evaluation**

389  
390 The estimated hourly FRE fields (or analysis;  $\hat{\rho}_t$ ) resulting from the two modelling approaches  
391 (persistent and climatological) were evaluated via comparison to those derived from the hourly  
392 SEVIRI time-series (see Sect. 2.1). Two criteria were used to evaluate model performance: first, the  
393 spatial distribution of FRE estimates; and second, the temporal distribution of FRE. The spatial  
394 performance of the modelling approaches was assessed via their ability to reproduce the annual  
395 mean FRE per land cover type, and by comparing the spatial distribution of FRE as estimated by the  
396 modelling approaches and as derived from SEVIRI over the study region and period. The temporal  
397 performance was assessed via the ability of the model to allocate the emitted energy in the right grid  
398 cell at the right moment in time. Here we used Pearson's r between the modelled and observed  
399 (SEVIRI) FRE time-series at four different spatiotemporal resolutions (0.1° and 1° spatial, and hourly  
400 and daily temporal resolution). Each spatiotemporal scale provides unique information on the model  
401 performance. Correlation coefficients at hourly resolution depend on the ability of the model to  
402 estimate the distribution of fire activity over the day, while daily aggregated estimates provide  
403 insights in the ability to get overall budgets right. In a similar way the two spatial resolutions provide  
404 information on the ability of the model to resolve high resolution distribution of fire activity and  
405 more regional model performance. When calculating Pearson's r between the hourly model results  
406 and SEVIRI data we included cloud free days only, while the daily model results were compared to  
407 the full cloud cover corrected SEVIRI times series, using a simple cloud cover correction method  
408 explained below.

409  
410 Finally, we compared daily regional aggregated FRE time-series for several study regions of the two  
411 modelling approaches and SEVIRI. In order to compare daily regional time-series to the model, a  
412 cloud cover correction needed to be carried out. Since persistent cloud cover is relatively rare during  
413 the burning season in most parts of Africa, we chose a simple gap filling approach where the value of  
414 the last cloud-free observation is assumed to be valid until the next cloud-free observation, which is  
415 consistent with the observation gap filling in the daily GFAS.

416

## 417 4 Results

418

### 419 4.1 The diurnal cycle and MODIS sampling

420

421 First, we present the results related to the spatial distribution of the fire diurnal cycle, and assess the  
422 impact of the fire diurnal cycle on active fire observations made at the times of the MODIS overpass.  
423 The spatial distribution of the fire diurnal cycle was explored by optimally fitting a Gaussian function  
424 to the hourly, 0.1° SEVIRI FRP time-series. Reasonable overall correlations between SEVIRI and the  
425 optimally fitted Gaussian functions were found (Pearson's  $r = 0.55$ ; weighted mean for all grid cells),  
426 while a Gaussian was better able to describe hourly fire activity in regions where fires could spread  
427 over large areas and were characterized by high  $\rho_{peak}$  (e.g., for fire size  $< 10 \text{ km}^2$   $r = 0.51$ , for  $10\text{--}50$   
428  $\text{km}^2$   $r = 0.56$ , and  $> 50 \text{ km}^2$   $r = 0.63$ ). This is likely to be in part related to the fact that characterisation  
429 of the diurnal cycle of "smaller" fires will be more affected by instances of SEVIRI failing to detect one  
430 or more of their fire pixels than would larger fires, hence introducing more variability into the  
431 apparent diurnal cycle. Whilst the SEVIRI FRP-PIXEL product shows apparently the best performance  
432 metrics of any current geostationary fire product derived from SEVIRI data (Baldassarre et al., 2015),  
433 such failures in active fire pixel detection clearly occur, for example simply due to fire pixels being  
434 too low in their FRP to detect by SEVIRI, along with a variety of potential other factors (Wooster et  
435 al., 2015).

436

437 Figure 1 shows an example of two 0.1° grid cells in which the hourly average FRP maxima reached  
438 relatively high levels, well in excess of 1 GW, and fire persisted for several days. As with the individual  
439 fires, shown by SEVIRI in Wooster et al. (2005) and Roberts et al. (2009), the FRP from these fires  
440 appears to drop to zero, or near zero, every night. This is a consequence both of the actual FRP from  
441 the fire significantly diminishing at this time due to, for example, fuel moisture, wind and other  
442 ambient atmospheric conditions being far less conducive to intense fire activity by night than by day  
443 (Hély et al., 2003; Gambiza et al., 2005), but also because some fire pixels will have FRPs below the  
444 SEVIRI active fire pixel detection limit of around 40 MW (Roberts and Wooster, 2008). At the start of  
445 the following day, fuel moisture and ambient atmospheric conditions generally become more  
446 conducive to fire, and fire intensities and rates of spread typically increase once more such that more  
447 of the fire-affected pixels breach the SEVIRI FRP detection limit (Roberts et al., 2009).

448

449 The results shown in Fig. 1 indicate that high FRP, relatively long-lived fire activity is rather well  
450 described by a Gaussian function, even at this 0.1°, hourly resolution which is significantly higher  
451 than that used in previous studies fitting Gaussian descriptors to remotely sensed measures of active  
452 fire activity. At the same time, it also became apparent that observations from a MODIS-type  
453 sampling interval are not always representative of the daily fire activity. The inability of the MODIS  
454 sampling times to provide representative observations is well illustrated in Fig. 1a, where on the first  
455 day of the fire the morning and afternoon time of MODIS sampling slot almost completely missed the  
456 fire activity.

457

458 The shape of the Gaussian function, and consequently the parameters: SD ( $\sigma$ ) peak fire activity ( $\rho_{peak}$ )  
459 and corresponding hour ( $h_{peak}$ ), varied considerably over the individual days (Fig. 1). For example, in

460 the African savanna grid cell (Fig. 1c), fire activity on day 3 continued longer in the afternoon  
461 compared to day 4, when conditions some-how became less favourable for maintaining the fire  
462 earlier in the afternoon. Therefore, the shape of the fire diurnal cycle is dependent on  
463 spatiotemporal scale. When diurnal fire activity was aggregated over several days, which can be  
464 compared to using a coarser temporal or spatial resolution, increased as compared to fire activity for  
465 individual days (compare Fig. 1a with b, and Fig. 1c with d). The relatively narrow diurnal cycle of the  
466 individual days have varying peak hours of fire activity, so that the sum of it is wider than any of the  
467 individual cycles and the peak fire activity less pronounced.

468

469 In addition to an observed variability in the fire diurnal cycle seen on different days, we found  
470 distinct spatial patterns in the optimal fitted Gaussian parameters (Fig. 2). Some of these patterns  
471 were similar for the different parameters. In particular, there were zones of generally more intense  
472 fires (e.g., South Sudan, northern Central African Republic, Botswana, Namibia and parts of Angola  
473 and the Democratic Republic of Congo (DRC)), showing relatively high values of  $\rho_{peak}$ ,  $\rho_{base}$  and  $\sigma$   
474 compared to other zones where values for all three parameters were relatively low (e.g., Zambia,  
475 Mozambique, Tanzania, Nigeria and Cameroon). On top of this general pattern, a clear gradient is  
476 visible as you move from drier to more humid regions, seen most clearly when moving from Namibia  
477 via Angola to DRC. In more humid savannas, when fuel conditions were optimal, high  $\rho_{peak}$  values  
478 could be reached but fire duration over the day was generally short and night time FRP values were  
479 more likely to fall below the SEVIRI FRP detection threshold (Fig. 2).  $h_{peak}$  varied considerably over the  
480 study region, with areas showing most fire activity late in the afternoon generally in more humid or  
481 forested regions but also in some more arid regions (Fig. 2d).

482

483 Table 1 shows the land cover-averaged values and SD of the results presented in Fig. 2. In addition  
484 we calculated the ratio of the mean SEVIRI FRP at MODIS daytime detection opportunities to the  
485 maximum daytime FRP  $\rho_{peak}$ . These results were used in the climatological modelling approach that  
486 combined the fire diurnal cycle climatology with observations made at the MODIS sampling times to  
487 derive the daily fire diurnal cycle predictions (Sect. 3.5). More intense fires with long duration and  
488 high peak values were associated with fires in shrublands, savannas and grasslands, while a more  
489 pronounced fire diurnal cycle was present in more humid woody savannas or tropical forests. For  $\sigma$ ,  
490  $\rho_{peak}$  and  $\rho_{base}$  SD was typically about half of the average value, while SD of  $h_{peak}$  was largest for  
491 temperate forests, shrublands and grasslands. The ratio of mean daytime FRP made at the MODIS  
492 sampling times and  $\rho_{peak}$  was relatively constant for various land cover types with  $\rho_{peak}$  generally  
493 about three times as large as the mean FRP at the daytime MODIS detection opportunities (Table 1).

494

495 In order to better understand the spatial distribution of the fire diurnal cycle features, we studied  
496 characteristics of the fire regime that were expected to be related to fuel properties and the diurnal  
497 cycle (Fig. 3a, c and d). To guide the interpretation we have included a land cover map, partly  
498 governing fuel loads, in Fig. 3b. Annual emitted FRE varied widely over the study region, and highest  
499 values were found in the savannas and woody savannas (compare Fig. 3a with b) and coincided with  
500 regions of large fire size and/or a high number of annual fire days (compare Fig. 3a with c and d).  
501 Similarities with characteristics of the fire diurnal cycle were also found, the earlier mentioned zones  
502 of generally more intense fires (high values of  $\rho_{peak}$ ,  $\rho_{base}$  and  $\sigma$ ) often coincided with regions of large  
503 fire size (Figs. 2a–c and 3c). In the more humid tropical areas, high  $\rho_{peak}$  values occurred in areas of  
504 relatively large fire size and/or a high number of annual fire days (Figs. 2a and 3c, d).

505  
506 The relative fraction of FRE emitted on days that SEVIRI data sampled at MODIS observation times  
507 did not observe active fires is an important factor affecting model performance, and showed similar  
508 spatial patterns as  $\sigma$ , indicating that duration of fires over the day plays an important role (Figs. 2c  
509 and 4a). In addition, the geographical location and cloud cover during the burning season played a  
510 role by affecting the effective number of daily MODIS observations (Fig. 4b). The peak hour of fire  
511 activity also played a role, and especially in more humid areas with frequent cloud cover and late  
512 afternoon fire activity sometimes over 50% of FRE was emitted on days without any SEVIRI active fire  
513 detections at MODIS detection opportunities (compare Figs. 2d and 4a). The most important biomass  
514 burning regions were typically characterized by relatively long fire duration over the day (Fig. 2c) and  
515 the effect of omission of active fires on continental scale FRE estimates was therefore relatively low  
516 (cf. Fig. 3a, 4a and 5). However, frequent omission of relatively small fires of short duration may  
517 strongly affect FRE estimates for some regions (Fig. 5). These results clearly demonstrate the value of  
518 the data provided by the very high temporal resolution geostationary systems, even though they are  
519 unable to resolve and detect fire pixels as low in FRP as those from polar orbiters (Roberts and  
520 Wooster, 2008).

521

## 522 **4.2 Model evaluation**

523

524 To evaluate the two modelling approaches that estimated FRE from SEVIRI data only at the MODIS  
525 sampling times we started with comparing the spatial distribution of mean estimated FRE for each  
526 method with the cloud corrected SEVIRI FRE calculated using the entire hourly, 0.1° SEVIRI FRP  
527 dataset (Fig. 5). The persistent approach resulted in a general overestimation of FRE, while the  
528 climatological approach showed overall good performance in terms of total estimated FRE when  
529 compared to the full SEVIRI dataset. Moreover, the more narrow distribution of modelled FRE as a  
530 fraction of SEVIRI FRE by the climatological approach as opposed to the persistent approach suggests  
531 that results are not only more accurate but also more precise (Fig. 5). While this reflects the general  
532 pattern, the performance bias was not homogeneous over the region. The persistent approach  
533 showed best results for regions with long daytime fire durations (i.e., large  $\sigma$ ) and with a late peak in  
534 fire activity; and although performing generally better, the climatological approach showed a general  
535 underestimation for areas of relatively late peak fire activity (compare Figs. 2 and 5). To a certain  
536 extent these regional differences correspond to the distribution of the different land cover types  
537 (Table 2). For example, for temperate forests and shrublands the persistent modelling approach  
538 showed notably better comparison to the FRE derived via the entire SEVIRI dataset, while the  
539 climatological modelling approach overestimated FRE.

540

541 Equally important as the absolute FRE estimates shown in Fig. 5 and Table 2 are their temporal  
542 dynamics. Figure 6 shows regional daily budgets for several study regions with different geographical  
543 positions and land cover. Similar to the results in Fig. 5, we found a general overestimation by the  
544 persistent approach, and better overall estimation by the climatological approach. Overestimation of  
545 the persistent approach was occurring mostly in the tropics (e.g., Nigeria and DRC), where also  
546 stronger day to day variability was observed as compared to that derived with the complete SEVIRI  
547 data or the other modelling approaches (Fig. 5). The climatological approach showed a small delay in  
548 FRE estimations compared to the complete SEVIRI dataset.

549

550 To further test the ability of the two modelling approaches to allocate FRE to the individual grid cells  
551 at the right moment in time, correlation coefficients were calculated. Table 3 shows Pearson's  $r$   
552 between SEVIRI and the two modelling approaches at four spatiotemporal resolutions (0.1° and 1°  
553 spatial and hourly and daily temporal resolution). A striking increase in correlation was observed  
554 when aggregating model results both temporally or spatially. Freeborn et al. (2009, 2011) previously  
555 demonstrated the value of such spatial aggregation when deriving relationships between SEVIRI and  
556 MODIS datasets, and this technique is currently used within the near real-time SEVIRI FRP-GRID  
557 products produced by the LSA SAF from the SEVIRI FRP-PIXEL data (Wooster et al., 2015). At 0.1°  
558 resolution the best correlations were found for shrublands and savannas while for aggregated data  
559 best performance was found for woody savannas and savannas. At hourly resolution, the  
560 climatological approach generally performed better than the persistent approach. However, at 0.1°  
561 daily the persistent approach performed best while at 1° spatial resolution the persistent and  
562 climatological approaches did equally well.

563

## 564 **5 Discussion**

565

566 Unlike biomass burning emission inventories based on burned area, inventories using active fire  
567 observations from Earth Observation satellites can be produced in near real time (Freitas et al., 2005;  
568 Reid et al., 2009; Sofiev et al., 2009; Wiedinmyer et al., 2011; Kaiser et al., 2012; Darmenov and da  
569 Silva, 2013). The near real time emissions inventories are, at present, generally based on active fire  
570 data from the MODIS instruments operating onboard the Terra and Aqua polar orbiting satellites.  
571 The FRP observations of MODIS are almost without saturation, operating day and night, with a  
572 reasonable spatial resolution and with new observations available for any location at least a few  
573 times every day – cloud cover permitting. However, it is well known that fire activity in most regions  
574 follows a clear daily cycle (e.g., Roberts et al., 2009; Vermote et al., 2009). Consequently, the FRP  
575 measures derived from intermittent polar orbiting MODIS observations are often not fully and  
576 directly representative of the actually daily fire activity (Fig. 1; Giglio, 2007; Vermote et al., 2009;  
577 Freeborn et al., 2011). Although several approaches have been developed to obtain more accurate  
578 estimations of FRE from the limited temporal sampling of FRP provided by MODIS (e.g., Ellicott et al.,  
579 2009; Freeborn et al., 2009, 2011; Vermote et al., 2009), they are all best suited to be used with  
580 previously collected and/or aggregated FRP data, and none can be readily implemented at high  
581 spatiotemporal resolution in near real time. For this reason, most current global emission inventories  
582 produced in near real time actually ignore fire diurnal dynamics completely (e.g., Kaiser et al., 2012),  
583 and this results in large biases in the FRE budgets (Ellicott et al., 2009; Zhang et al., 2012).

584

585 Here we start discussing the spatial distribution of the fire diurnal cycle, and its drivers (Sect. 5.1).  
586 Building on previous work, we explored two new methods to estimate hourly FRE in near real time  
587 from observations made by SEVIRI at MODIS detection opportunities. The results illustrate how  
588 MODIS observations might be used to calculate hourly FRE, and where errors can be expected due to  
589 the diurnal cycle and the limited temporal sampling provided by MODIS (Sect. 5.2).

590

## 591 **5.1 Exploring the fire diurnal cycle using a Gaussian function**

592

593 The fire diurnal cycle characteristics were explored by fitting of a Gaussian function to the hourly  
594 SEVIRI time-series. Vermote et al. (2009) and Ellicott et al. (2009) found that at a 0.5° monthly  
595 resolution the fire diurnal cycle can be described by a Gaussian function, using MODIS observations  
596 to resolve the unknown parameters. They choose the spatiotemporal size of the study regions such  
597 that a statistical representative number of fires and MODIS FRP detections were included, and the  
598 observations covered the full range of MODIS view angles – since the sensitivity of MODIS to fire  
599 depends upon this (Vermote et al., 2009). Although later work showed that in fact fire activity may  
600 be somewhat skewed in the afternoon, here we found that even at a high spatiotemporal resolution  
601 (0.1°; hourly) a Gaussian function provides a fairly robust description of the fire diurnal cycle.  
602 However, at 0.1° hourly resolution, SEVIRI data sampled at the MODIS detection opportunities does  
603 not always provide enough information to adequately depict fire activity for an individual grid cell  
604 and day (Fig. 1). Moreover, the spatiotemporal scale at which we observe the fire diurnal cycle has a  
605 significant impact on its shape. When moving to a coarser spatiotemporal resolution, the shape of  
606 the diurnal cycle likely becomes wider, with less pronounced peaks. This is mostly a consequence of  
607 the spatiotemporal variation in hour of peak fire activity of the individual fires or fire days (Fig. 1).  
608 Therefore, typical values of the parameters of the Gaussian found in this study (Fig. 2) do not  
609 necessarily correspond to typical values found by earlier studies (e.g., Roberts et al., 2009; Vermote  
610 et al., 2009), who used much larger sample sizes (i.e., spatiotemporal resolutions). Likewise the  
611 results presented here are not necessarily representative for individual fires.

612

613 Although the shape of the “average” fire diurnal cycle is scale dependent, regional patterns in the  
614 diurnal cycle characteristics (Fig. 2) remain similar over different scales, and therefore we found  
615 similar land cover dependent characteristics as previous studies. For example, shrublands and  
616 grasslands generally faced drier conditions when burning than did woody savannas or tropical forest,  
617 and therefore fire activity typically continued longer over the day and the hour of peak fire activity  
618 was generally located later in the afternoon (Fig. 2; Table 1; Giglio, 2007; Roberts et al., 2009). For  
619 the same reason, temperate and boreal forests have been reported to show a more pronounced  
620 diurnal cycle than grasslands (Fig. 2; Sofiev et al., 2013; Konovalov et al., 2014). Building on the land  
621 cover based analysis of Roberts et al. (2009), we provide a first analysis of the spatial distribution of  
622 the fire diurnal cycle.

623

624 The three parameters determining the shape of the Gaussian can be used to visualize the spatial  
625 distribution of the fire diurnal cycle. The daily FRP-maximum is given by  $\rho_{peak}$ , fire duration over the  
626 day by  $\sigma$ , and the baseline FRP by  $\rho_{base}$ . Similar spatial patterns were found for all three parameters  
627 mentioned above (Fig. 2a, b and c). This indicates that there are zones of generally more “intense”  
628 fires with high  $\rho_{peak}$ , large  $\sigma$  and higher  $\rho_{base}$ , while other zones are characterised by lower intensity  
629 fires. In land cover classes where most of the fires were grass fuelled (grasslands, savannas and  
630 woody savannas), a considerable part of the spatial variation in fire diurnal cycle could be explained  
631 by fire size (see Sect. 2.4; Figs. 2 and 3). Large fires were often found in frequently burnt and/or more  
632 arid areas (Fig. 3a) where high fuel connectivity, low fuel density and low fuel moisture allow  
633 relatively fast moving fires with large fire fronts to form (Hély et al., 2003; Sow et al., 2013). Besides  
634 fire size and land cover, part of the variability in the fire diurnal cycle could be explained by a  
635 gradient in diurnal weather conditions. Grass fuelled large fires were also common in the more

636 humid savannas of southern Africa, but here nighttime weather conditions appear to become rather  
637 unfavourable for fire (Figs. 2b and 3c). In humid savannas  $\rho_{peak}$  values were not solely associated with  
638 large fire size, but also with areas showing a high number of annual days with fire activity and may be  
639 explained by several relatively small fires burning at the time. The high number of fire days may  
640 indicate a larger number of fire ignitions and/or that fires are spreading at a slower rate due to the  
641 more pronounced fire diurnal cycle, higher humidity, or higher fuel density (Hély et al., 2003; Sow et  
642 al., 2013). Finally, in the Mediterranean basin the relatively low fire return period, and consequently  
643 higher fuel density, may also cause relative intense fires with long duration over the day (Fig. 2;  
644 Archibald et al., 2013).

645  
646 The peak hour of fire activity found here corresponds to the moment of day at which 50% of the total  
647 FRE has been emitted (assuming  $\rho_{base} \ll \rho_{peak}$ ), and it did not always correspond to the peak hour  
648 of fire activity found by previous studies (Fig. 2d; e.g., Giglio, 2007; Roberts et al., 2009; Vermote et  
649 al., 2009). In general most FRE was emitted during the afternoon, and clear spatial patterns were  
650 present in the typical peak hour of the Gaussian. High values of  $h_{peak}$  were found in regions of higher  
651 fuel density or in more arid areas where fires could spread over large areas (Figs. 2d and 3). In arid  
652 regions with large typical fire sizes, fire spread was often fast and a 0.1° grid cell only corresponded  
653 to a part of the actual fire resulting in large variation in  $h_{peak}$  between neighbouring grid cells (Fig. 2d  
654 and Table 1).  
655

## 656 **5.2 Model performance and the MODIS sampling design**

657  
658 Data assimilation and two modelling approaches, were used to estimate hourly FRE from SEVIRI FRP  
659 data sampled at the times of MODIS detection opportunities. Here we start discussing the  
660 performance of the different methods with respect to their total FRE estimates and daily regional  
661 FRE estimations. Then we discuss the more uncertain model performance at higher spatiotemporal  
662 resolutions.

663  
664 The persistent approach is comparable to a direct hourly extension of the current GFAS methods  
665 (Kaiser et al., 2012), where the fire diurnal cycle is ignored and the predicted FRP for each hour is  
666 equal to that of the last FRP observation. This led to a general overestimation of daily FRE because  
667 the 13:30 LT temporal sampling time of MODIS is relatively close to the peak hour of daily fire  
668 activity, and therefore not very representative of the full period until the next observation at 22:30  
669 LT (Figs. 2d and 5; Table 2). Moving away from the equator, the number of daily MODIS observations  
670 increases due to orbital convergence at higher latitudes, and consequently the model performance  
671 improved (Figs. 4b, 5 and 6; Giglio et al., 2006; Reid et al., 2009). Additional inclusion of daytime  
672 observations due to orbital convergence will typically be somewhat earlier or later in the afternoon  
673 and may therefore lower the FRE estimation. In the persistent approach, missing nighttime  
674 observations may cause an overestimation and missing daytime observation an underestimation of  
675 daily FRE, resulting in erroneous regional day-to-day variations in FRE estimates in the tropics (Fig. 6).  
676 Following previous research, we found that due to the spatiotemporal variation of the fire diurnal  
677 cycle FRE was overestimated more for some land cover types than for others (Table 2; Freeborn et  
678 al., 2011). Land cover classes that typically showed longer fire durations (Fig. 2c) with peak fire  
679 activity later in the afternoon (Fig. 2d) were not as much overestimated as land cover classes with

680 more pronounced fire diurnal cycles (Figs. 5 and 6; Table 2). However, part of this effect likely stems  
681 from these land covers mostly being located in the more frequently observed higher latitudes of our  
682 study region. Although the persistent method is not directly comparable to the methods of widely  
683 used emission inventories like GFAS or QFED (Kaiser et al., 2012; Darmenov and da Silva, 2013), they  
684 likely introduce similar errors by ignoring the fire diurnal cycle.

685  
686 The climatological approach showed better performance in terms of absolute FRE estimations, while  
687 also better able to reproduce its spatial variability (Fig. 5). In contrast to the persistent approach, the  
688 hourly predictions were based on the last 24h of fire activity, enabling more realistic gap filling during  
689 periods without observations. This resulted in an advantage during periods of cloud cover or missing  
690 observations due to the satellite orbits, but because of the low number of actual daily observations  
691 the climatological approach had the tendency to continue predicting fire activity after fires had  
692 ceased, seen as a small delay in the signals in Fig. 6.

693  
694 An additional criterion to evaluate the model performance was the correlation between the  
695 modelling approaches and the SEVIRI data at different spatiotemporal scales. Correlation between  
696 the modelled and SEVIRI time-series improved considerably when moving from hourly to daily  
697 resolution, showing that the models were better able to estimate daily budgets than the distribution  
698 of fire activity over the day. These differences may be explained by the inability of the models to  
699 correctly estimate the hour of peak fire activity, a fire diurnal cycle that is not well represented by a  
700 Gaussian function, or in the case of small fires the fire diurnal cycle may not be fully detected by the  
701 SEVIRI instrument. Because of the large day-to-day variation in the fire diurnal cycle and the FRP  
702 measurements limited to the time of the MODIS overpasses, the individual FRP observations have a  
703 low precision (i.e., large random error) and omission (i.e., non detection) of fires is frequent (Figs. 1  
704 and 4), resulting in low correlation at high spatiotemporal scales (Table 3). Because fires rarely occur  
705 on their own and generally form part of a regional pattern (Bella et al., 2006), the correlation  
706 increased considerably when accumulating results to a 1° spatial scale. For the same reason model  
707 performance was found to be best in savannas and woody savannas, where the highest number of  
708 fires occur and the sample size is thus largest, or in areas of large fire size where omission was  
709 relatively low. Model performance was therefore best when optimal burning conditions were  
710 reached, often coinciding with the peak of the burning season. Because often only a reasonably large  
711 sample of observations made at the MODIS detection opportunities is actually representative of fire  
712 activity in a certain region, the added value of the 0.1° spatial resolution (e.g., GFASv1.1/1.2) is  
713 somewhat limited compared to a coarser 0.5° spatial resolution (e.g., GFASv1.0).

714  
715 Overall, using the climatological approach resulted in the best model performance, although in  
716 specific cases using the persistent approach showed better results. For example, at 0.1° spatial and  
717 daily temporal resolution the persistent approach performed best, likely because it only predicts fire  
718 activity on days of actual fires while the climatological approach may predict fire activity with some  
719 delay. Also the climatological approach used mean values for the fire duration and may therefore  
720 overestimate FRE from smaller fires while underestimating the larger fires. Despite the improved  
721 results of the climatological approach as opposed to the persistent approach, estimating FRE in near  
722 real time based on MODIS observations remains challenging, especially at high spatiotemporal  
723 resolutions. Largest uncertainties originate from the high spatiotemporal variability of the fire diurnal  
724 cycle combined with the limited number of daily MODIS detection opportunities. Moreover, the fire

725 diurnal cycle as analyzed here may to some extent be affected by the inability of SEVIRI to detect the  
726 smallest fires, along with other sources of uncertainty in the FRP observations (Wooster et al., 2015;  
727 Roberts et al., 2015). Finally, the characterization of the fire diurnal cycle and discussion of its  
728 spatiotemporal drivers presented here provide a first step to upscale the climatological model to a  
729 global scale, but a better understanding of the fire diurnal cycle and its drivers for other regions of  
730 the globe remains an important issue.

731  
732 Within GFAS, to handle the uncertainties introduced into the MODIS-derived FRE estimates by  
733 neglecting the diurnal cycle influence, the estimated FRE is converted into estimates of dry matter  
734 burned (DM) using land cover-specific conversion factors. These were derived via comparison of  
735 long-term monthly FRE estimates to the DM estimates calculated over the same period by the Global  
736 Fire Emissions Database (GFED 3.1; van der Werf et al., 2010; Kaiser et al., 2012). It is currently  
737 assumed that by allowing the conversion factors to vary with land cover type the impact of any land  
738 cover-varying diurnal cycle is also incorporated, reducing the influence of the diurnal cycle. The  
739 issues discussed above, along with the accuracy of the GFED DM calculations, which are for example  
740 affected by the quality of the burned area product and the biochemical models used, all influence  
741 values of the land cover-specific FRE-to-DM conversions factors presented by Kaiser et al. (2012).

742  
743 Wooster et al. (2005) and Freeborn et al. (2008) previously explored the conversion factors between  
744 FRE and DM using small scale experiments, and found that they appeared relatively independent of  
745 vegetation type. However, when moving to the satellite-scale there are additional factors influencing  
746 this FRE-to-DM relationship, for example the fire regime of an area and the degree to which MODIS  
747 misses the lowest FRP fires, and the canopy density of trees that might obscure some of the thermal  
748 radiation being emitted by fires burning in the ground fuels (Freeborn et al., 2014). The thermal  
749 radiation recorded in satellite products is additionally reduced by cloud cover and erroneous flagging  
750 of smoke as clouds during data processing. Konovalov et al. (2014) nevertheless found FRE-to-DM  
751 relationships relatively similar to those of the earlier small-scale experiments when using  
752 atmospheric observations and biomass burning trace gas and aerosol emissions factors to estimate  
753 fuel consumption. Exploring methods to incorporate the fire diurnal cycle in the GFAS global FRP-  
754 based near real time emission inventory is a first step in taking into account some of these issues in  
755 order to improve global FRE estimates made at relatively high spatiotemporal resolutions, and  
756 hopefully also in reconciling some of the differences in current emission inventories.

757

## 758 **6 Conclusions**

759  
760 Emission inventories based on FRP observations have great potential to improve biomass burning  
761 emission estimates, by eliminating the need for modelling of fuel loads and fuel consumption, and  
762 can be produced in near real time. However, to date uncertainties in FRE estimation remain high  
763 when using polar orbiting FRP datasets, largely due to difficulties in combining the limited temporal  
764 resolution observations and knowledge about the fire diurnal cycle. Geostationary data can alleviate  
765 this issue, but brings its own problems related to the non-detection of the lower FRP fires due to the  
766 coarse spatial resolution of the geostationary observations. Geostationary dataset are also not global  
767 in extent. Here we explored the spatial dependencies of the fire diurnal cycle and its impact on active  
768 fire detections made at the time of MODIS overpasses. Two modelling approaches were developed

769 to derive hourly FRE estimates based on data-assimilation and SEVIRI FRP observations subsampled  
770 at MODIS detection opportunities. The first approach ignored the fire diurnal cycle assuming  
771 persistent fire activity between two MODIS detection opportunities, while the second approach  
772 combined prior knowledge of the fire diurnal cycle with active fire observations at MODIS detection  
773 opportunities to simulate the fire diurnal cycle. Both approaches were evaluated against the actual  
774 hourly FRP observations made by SEVIRI. Our main conclusions are:

- 775 1. We considered various drivers of the spatial distribution of fire diurnal cycle: dominant land  
776 cover, fire size, annual number of fire days, and diurnal climate conditions and found that all  
777 played a role. The strong relation between fire size and fire diurnal cycle for grass fuelled  
778 fires, and the climatic gradient in diurnal cycle, indicate that using fuel characteristics rather  
779 than land cover alone to characterize the fire diurnal cycle provides a potential pathway to  
780 improve these estimates. Here we showed that this information can partly be obtained by  
781 studying the fire characteristics, such as fire size, which are contained within the remote  
782 sensing data themselves.
- 783 2. Ignoring the fire diurnal cycle may cause structural errors in FRE estimates, and likely results  
784 in a general overestimation of FRE due to the timing of the MODIS overpasses. The errors  
785 vary regionally, mostly due to variations in the fire diurnal cycle, while results get more  
786 accurate at higher latitudes due to the increasing number of daily MODIS detection  
787 opportunities caused by orbital convergence.
- 788 3. Due to the large day-to-day variations in the fire diurnal cycle at the grid cell level, and the  
789 scarce number of MODIS observations of any one location per day, daily FRP fields calculated  
790 from observations made at MODIS detection opportunities are characterized by low  
791 precision (i.e., observations are not representative for daily fire activity) and high omission  
792 (i.e., non observation of fires). Therefore a sufficiently large sample size of MODIS  
793 observations is required to accurately estimate FRE, as shown earlier by Freeborn et al.  
794 (2011). In zones of frequent fires, where fires are generally part of a regional biomass  
795 burning pattern, model performance greatly improved when moving to a coarser scale,  
796 increasing the sample size. Model performance was also considerably better for zones of  
797 relatively large fires that were characterized by low omission. Production of emission  
798 inventories at very high spatiotemporal resolution using data from a limited number of low-  
799 Earth orbit satellite observations may therefore provide somewhat restricted added value  
800 compared to those derived at coarser spatiotemporal scales.
- 801 4. Relative overrepresentation of day- or nighttime FRP observations may cause large day to  
802 day variations in estimated FRE when the diurnal cycle is ignored.
- 803 5. The way we observe the fire diurnal cycle is scale dependent, mostly because of the large  
804 variation in fire diurnal cycle, even within the same grid cell between different days.

806 We recommend implementing the climatological model within GFAS in Copernicus Atmosphere  
807 Services in order to improve global and regional FRE estimates and further reconcile emission  
808 estimates from the various different inventories currently available.

#### 810 **Acknowledgements.**

811 We like to thank Samuel Remy at ECMWF for processing MODIS and SEVIRI data, and the data  
812 providing agencies: NASA and the EUMETSAT LSA SAF for making their data publicly available. This

813 study was funded by the EU in the FP7 and H2020 projects MACC-II and MACC-III (contracts no.  
814 283576 and 633080).

815

## 816 **References**

817

818 Archibald, S. and Roy, D. P.: Identifying individual fires from satellite-derived burned area data, IEEE  
819 Int. Geosci. Remote Sens. Symp. Proc., 9, 160–163, doi:10.1109/IGARSS.2009.5417974, 2009.

820

821 Archibald, S., Lehmann, C. E. R., Gómez-Dans, J. L., and Bradstock, R. A.: Defining pyromes and global  
822 syndromes of fire regimes, P. Natl. Acad. Sci. USA, 110, 6442–6447, doi:10.1073/pnas.1211466110,  
823 2013.

824

825 Baldassarre, G., Pozzoli, L., Schmidt, C. C., Unal, A., Kindap, T., Menzel, W. P., Whitburn, S., Coheur,  
826 P.-F., Kavgaci, A., and Kaiser, J. W.: Using SEVIRI fire observations to drive smoke plumes in the CMAQ  
827 air quality model: the case of Antalya in 2008, Atmos. Chem. Phys. Discuss., 15, 1–46,  
828 doi:10.5194/acpd-15-1-2015, 2015.

829

830 Bella, C. M., Jobbagy, E. G., Paruelo, J. M., and Pinnock, S.: Continental fire density patterns in South  
831 America, Global Ecol. Biogeogr., 15, 192–199, doi:10.1111/j.1466-822X.2006.00225.x, 2006.

832

833 Boschetti, L. and Roy, D. P.: Strategies for the fusion of satellite fire radiative power with burned area  
834 data for fire radiative energy derivation, J. Geophys. Res., 114, D20302, doi:10.1029/2008JD011645,  
835 2009.

836

837 Bowman, D. M. J. S., Balch, J. K., Artaxo, P., Bond, W. J., Carlson, J. M., Cochrane, M. A., D'Antonio, C.  
838 M., Defries, R. S., Doyle, J. C., Harrison, S. P., Johnston, F. H., Keeley, J. E., Krawchuk, M. A., Kull, C. A.,  
839 Marston, J. B., Moritz, M. A., Prentice, I. C., Roos, C. I., Scott, A. C., Swetnam, T. W., van der Werf, G.  
840 R., and Pyne, S. J.: Fire in the Earth system, Science, 324, 481–484, doi:10.1126/science.1163886,  
841 2009.

842

843 Darmenov, A. S. and da Silva, A.: The Quick Fire Emissions Dataset (QFED) – Documentation of  
844 Versions 2.1, 2.2 and 2.4, NASA Tech. Rep. Ser. Glob. Model. Data Assim., Greenbelt, USA, 32, 2013.

845

846 Ellicott, E., Vermote, E., Giglio, L., and Roberts, G.: Estimating biomass consumed from fire using  
847 MODIS FRE, Geophys. Res. Lett., 36, L13401, doi:10.1029/2009GL038581, 2009.

848

849 Freeborn, P. H., Wooster, M. J., Hao, W. M., Ryan, C. A., Nordgren, B. L., Baker, S. P., and Ichoku, C.:  
850 Relationships between energy release, fuel mass loss, and trace gas and aerosol emissions during  
851 laboratory biomass fires, J. Geophys. Res., 113, D01301, doi:10.1029/2007JD008679, 2008.

852

853 Freeborn, P. H., Wooster, M. J., Roberts, G., Malamud, B. D., and Xu, W.: Development of a virtual  
854 active fire product for Africa through a synthesis of geostationary and polar orbiting satellite data,  
855 Remote Sens. Environ., 113, 1700–1711, doi:10.1016/j.rse.2009.03.013, 2009.

856

857 Freeborn, P. H., Wooster, M. J., and Roberts, G.: Addressing the spatiotemporal sampling design of  
858 MODIS to provide estimates of the fire radiative energy emitted from Africa, *Remote Sens. Environ.*,  
859 115, 475–489, doi:10.1016/j.rse.2010.09.017, 2011.

860

861 Freeborn, P. H., Wooster, M. J., Roberts, G., and Xu, W.: Evaluating the SEVIRI fire thermal anomaly  
862 detection algorithm across the Central African Republic using the MODIS active fire product, *Remote*  
863 *Sens. Environ.*, 6, 1890–1917, doi:10.3390/rs6031890, 2014.

864

865 Freitas, S. R., Longo, K. M., Silva Dias, M. A. F., Silva Dias, P. L., Chatfield, R., Prins, E., Artaxo, P., Grell,  
866 G. A., and Recuero, F. S.: Monitoring the transport of biomass burning emissions in South America,  
867 *Environ. Fluid Mech.*, 5, 135–167, doi:10.1007/s10652-005-0243-7, 2005.

868

869 Friedl, M. A., McIver, D. K., Hodges, J. C. F., Zhang, X. Y., Muchoney, D., Strahler, A. H., Woodcock, C.  
870 E., Gopal, S., Schneider, A., Cooper, A., Baccini, A., Gao, F., and Schaaf, C.: Global land cover mapping  
871 from MODIS: algorithms and early results, *Remote Sens. Environ.*, 83, 287–302, doi:10.1016/S0034-  
872 4257(02)00078-0, 2002.

873

874 Gambiza, J., Campbell, B. M., Moe, S. R., and Frost, P. G. H.: Fire behaviour in a semi-arid *Baikiaea*  
875 *plurijuga* savanna woodland on Kalahari sands in western Zimbabwe, *S. Afr. J. Sci.*, 101, 239–244,  
876 2005.

877

878 Giglio, L.: Characterization of the tropical diurnal fire cycle using VIRS and MODIS observations,  
879 *Remote Sens. Environ.*, 108, 407–421, doi:10.1016/j.rse.2006.11.018, 2007.

880

881 Giglio, L., Justice, C. O., and Csiszar, I.: Global distribution and seasonality of active fires as observed  
882 with the Terra and Aqua Moderate Resolution Imaging Spectroradiometer (MODIS) sensors, *J.*  
883 *Geophys. Res.*, 111, G02016, doi:10.1029/2005JG000142, 2006.

884

885 Giglio, L., Loboda, T., Roy, D. P., Quayle, B., and Justice, C. O.: An active-fire based burned area  
886 mapping algorithm for the MODIS sensor, *Remote Sens. Environ.*, 113, 408–420,  
887 doi:10.1016/j.rse.2008.10.006, 2009.

888

889 Giglio, L., Randerson, J. T., and van der Werf, G. R.: Analysis of daily, monthly, and annual burned  
890 area using the fourth-generation global fire emissions database (GFED4), *J. Geophys. Res.-Biogeo.*,  
891 118, 317–328, doi:10.1002/jgrg.20042, 2013.

892

893 Hély, C., Alleaume, S., Swap, R. J., Shugart, H. H., and Justice, C. O.: SAFARI-2000 characterization of  
894 fuels, fire behavior, combustion completeness, and emissions from experimental burns in infertile  
895 grass savannas in western Zambia, *J. Arid Environ.*, 54, 381–394, doi:10.1006/jare.2002.1097, 2003.

896

897 Ichoku, C., Giglio, L., Wooster, M. J., and Remer, L. A.: Global characterization of biomass-burning  
898 patterns using satellite measurements of fire radiative energy, *Remote Sens. Environ.*, 112, 2950–  
899 2962, doi:10.1016/j.rse.2008.02.009, 2008.

900

901 Johnston, F. H., Henderson, S. B., Chen, Y., Randerson, J. T., Marlier, M., Defries, R. S., Kinney, P.,  
902 Bowman, D. M. J. S., and Brauer, M.: Estimated global mortality attributable to smoke from  
903 landscape fires, *Environ. Health Persp.*, 120, 695–701, doi:10.1289/ehp.1104422, 2012.  
904  
905 Kaiser, J. W., Flemming, J., Schultz, M. G., Suttie, M., and Wooster, M. J.: The MACC Global Fire  
906 Assimilation System: First Emission Products (GFASv0), Tech. Memo. 596, ECMWF, Reading, UK,  
907 2009.  
908  
909 Kaiser, J. W., Heil, A., Andreae, M. O., Benedetti, A., Chubarova, N., Jones, L., Morcrette, J.-J.,  
910 Razinger, M., Schultz, M. G., Suttie, M., and van der Werf, G. R.: Biomass burning emissions  
911 estimated with a global fire assimilation system based on observed fire radiative power,  
912 *Biogeosciences*, 9, 527–554, doi:10.5194/bg-9-527-2012, 2012.  
913  
914 Konovalov, I. B., Berezin, E. V., Ciais, P., Broquet, G., Beekmann, M., Hadji-Lazaro, J., Cler-baux, C.,  
915 Andreae, M. O., Kaiser, J. W., and Schulze, E.-D.: Constraining CO<sub>2</sub> emissions from open biomass  
916 burning by satellite observations of co-emitted species: a method and its application to wildfires in  
917 Siberia, *Atmos. Chem. Phys.*, 14, 10383–10410, doi:10.5194/acp-14-10383-2014, 2014.  
918  
919 Langmann, B., Duncan, B., Textor, C., Trentmann, J., and van der Werf, G. R.: Vegetation fire  
920 emissions and their impact on air pollution and climate, *Atmos. Environ.*, 43, 107–116,  
921 doi:10.1016/j.atmosenv.2008.09.047, 2009.  
922  
923 Larkin, N. K., Rause, S. M., and Strand, T. M.: Wildland fire emissions, carbon, and climate: US  
924 emissions inventories, *Forest Ecol. Manag.*, 317, 61–69, doi:10.1016/j.foreco.2013.09.012, 2014.  
925  
926 Mu, M., Randerson, J. T., van der Werf, G. R., Giglio, L., Kasibhatla, P., Morton, D. C., Collatz, G. J.,  
927 DeFries, R. S., Hyer, E. J., Prins, E. M., Grith, D. W. T., Wunch, D., Toon, G. C., Sherlock, V., and  
928 Wennberg, P. O.: Daily and 3 hourly variability in global fire emissions and consequences for  
929 atmospheric model predictions of carbon monoxide, *J. Geophys. Res.-Atmos.*, 116, D24303,  
930 doi:10.1029/2011JD016245, 2011.  
931  
932 Prins, E. M. and Menzel, W. P.: Geostationary satellite detection of biomass burning in South  
933 America, *Int. J. Remote Sens.*, 13, 2783–2799, doi:10.1080/01431169208904081, 1992.  
934  
935 Randerson, J. T., Chen, Y., van der Werf, G. R., Rogers, B. M., and Morton, D. C.: Global burned area  
936 and biomass burning emissions from small fires, *J. Geophys. Res.*, 117, G04012,  
937 doi:10.1029/2012JG002128, 2012.  
938  
939 Reid, J. S., Hyer, E. J., Prins, E. M., Westphal, D. L., Zhang, J., Wang, J., Christopher, S. A., Curtis, C. A.,  
940 Schmidt, C. C., Eleuterio, D. P., Richardson, K. A., and Homan, J. P.: Global monitoring and forecasting  
941 of biomass-burning smoke: description of and lessons from the Fire Locating and Modeling of  
942 Burning Emissions (FLAMBE) program, *IEEE J. Sel. Top. Appl.*, 2, 144–162,  
943 doi:10.1109/JSTARS.2009.2027443, 2009.  
944

945 Roberts, G. J. and Wooster, M. J.: Fire detection and fire characterization over Africa using meteosat  
946 SEVIRI, *IEEE T. Geosci. Remote*, 46, 1200–1218, doi:10.1109/TGRS.2008.915751, 2008.  
947

948 Roberts, G., Wooster, M. J., Perry, G. L. W., Drake, N., Rebelo, L.-M., and Dipotso, F.: Retrieval of  
949 biomass combustion rates and totals from fire radiative power observations: application to southern  
950 Africa using geostationary SEVIRI imagery, *J. Geophys. Res.*, 110, D21111,  
951 doi:10.1029/2005JD006018, 2005.  
952

953 Roberts, G., Wooster, M. J., and Lagoudakis, E.: Annual and diurnal african biomass burning temporal  
954 dynamics, *Biogeosciences*, 6, 849–866, doi:10.5194/bg-6-849-2009, 2009.  
955

956 Roberts, G., Wooster, M. J., Freeborn, P. H., and Xu, W.: Integration of geostationary FRP and polar-  
957 orbiter burned area datasets for an enhanced biomass burning inventory, *Remote Sens. Environ.*,  
958 115, 2047–2061, doi:10.1016/j.rse.2011.04.006, 2011.  
959

960 Roberts, G., Wooster, M. J., Xu, W., Freeborn, P. H., Morcrette, J.-J., Jones, L., Benedetti, A., and  
961 Kaiser, J. W.: Meteosat SEVIRI Fire Radiative Power (FRP) products from the Land Surface Analysis  
962 Satellite Applications Facility (LSA SAF) – Part 2: Product evaluation and demonstration of use within  
963 the Copernicus Atmosphere Monitoring Service, *Atmos. Chem. Phys. Discuss.*, 15, 15909–15976,  
964 doi:10.5194/acpd-15-15909-2015, 2015.  
965

966 Roy, D. P., Jin, Y., Lewis, P. E., and Justice, C. O.: Prototyping a global algorithm for systematic fire-  
967 affected area mapping using MODIS time series data, *Remote Sens. Environ.*, 97, 137–162,  
968 doi:10.1016/j.rse.2005.04.007, 2005.  
969

970 Schmetz, J., Pili, P., Tjemkes, S., Just, D., Kerkmann, J., Rota, S., and Ratier, A.: An introduction to  
971 Meteosat Second Generation (MSG), *B. Am. Meteorol. Soc.*, 83, 977–991, doi:10.1175/BAMS-83-7-  
972 Schmetz-1, 2002.  
973

974 Seiler, W., and Crutzen, P. J.: Estimates of gross and net fluxes of carbon between the biosphere and  
975 the atmosphere from biomass burning, *Climatic Change*, 2, 207–247, doi:10.1007/BF00137988, 1980.  
976

977 Sofiev, M., Vankevich, R., Lotjonen, M., Prank, M., Petukhov, V., Ermakova, T., Koskinen, J., and  
978 Kukkonen, J.: An operational system for the assimilation of the satellite information on wild-land fires  
979 for the needs of air quality modelling and forecasting, *Atmos. Chem. Phys.*, 9, 6833–6847,  
980 doi:10.5194/acp-9-6833-2009, 2009.  
981

982 Sofiev, M., Vankevich, R., Ermakova, T., and Hakkarainen, J.: Global mapping of maximum emission  
983 heights and resulting vertical profiles of wildfire emissions, *Atmos. Chem. Phys.*, 13, 7039–7052,  
984 doi:10.5194/acp-13-7039-2013, 2013.  
985

986 Sow, M., Hély, C., Mbow, C., and Sambou, B.: Fuel and fire behavior analysis for early-season  
987 prescribed fire planning in Sudanian and Sahelian savannas, *J. Arid Environ.*, 89, 84–93,  
988 doi:10.1016/j.jaridenv.2012.09.007, 2013.  
989

990 van der Werf, G. R., Randerson, J. T., Giglio, L., Collatz, G. J., Mu, M., Kasibhatla, P. S., Morton, D. C.,  
991 DeFries, R. S., Jin, Y., and van Leeuwen, T. T.: Global fire emissions and the contribution of  
992 deforestation, savanna, forest, agricultural, and peat fires (1997–2009), *Atmos. Chem. Phys.*, 10,  
993 11707–11735, doi:10.5194/acp-10-11707-2010, 2010.

994

995 Vermote, E., Ellicott, E., Dubovik, O., Lapyonok, T., Chin, M., Giglio, L., and Roberts, G. J.: An approach  
996 to estimate global biomass burning emissions of organic and black carbon from MODIS fire radiative  
997 power, *J. Geophys. Res.*, 114, D18205, doi:10.1029/2008JD011188, 2009.

998

999 Wiedinmyer, C., Akagi, S. K., Yokelson, R. J., Emmons, L. K., Al-Saadi, J. A., Orlando, J. J., and Soja, A.  
1000 J.: The Fire INventory from NCAR (FINN): a high resolution global model to estimate the emissions  
1001 from open burning, *Geosci. Model Dev.*, 4, 625–641, doi:10.5194/gmd-4-625-2011, 2011.

1002

1003 Wooster, M. J., Roberts, G., Perry, G. L. W., and Kaufman, Y. J.: Retrieval of biomass combustion rates  
1004 and totals from fire radiative power observations: FRP derivation and calibration relationships  
1005 between biomass consumption, *J. Geophys. Res.*, 110, D24311, doi:10.1029/2005JD006318, 2005.

1006

1007 Wooster, M. J., Roberts, G. J., Freeborn, P. H., Xu, W., Govaerts, Y., Beedy, R., He, J., and Mullen, R.:  
1008 Meteosat SEVIRI Fire Radiative Power (FRP) products from the Land Surface Analysis Satellite  
1009 Applications Facility (LSA SAF) – Part 1: Algorithms, product contents and analysis, *Atmos. Chem.*  
1010 *Phys. Discuss.*, 15, 15831–15907, doi:10.5194/acpd-15-15831-2015, 2015.

1011

1012 Xu, W., Wooster, M. J., Roberts, G., and Freeborn, P.: New GOES imager algorithms for cloud and  
1013 active fire detection and fire radiative power assessment across North, South and Central America,  
1014 *Remote Sens. Environ.*, 114, 1876–1895, doi:10.1016/j.rse.2010.03.012, 2010.

1015

1016 Zhang, X., Kondragunta, S., Ram, J., Schmidt, C., and Huang, H.-C.: Near-real-time global biomass  
1017 burning emissions product from geostationary satellite constellation, *J. Geophys. Res.*, 117, D14201,  
1018 doi:10.1029/2012JD017459, 2012.

1019

1020 Table 1. Mean values of the parameters of the Gaussian function per land cover type (excluding days  
 1021 of cloud cover and weighted by FRE), SD are shown in parenthesis. Values of  $\sigma$  and the ratio of  $\rho_{peak}$   
 1022 and mean day-time FRP at MODIS detection opportunities ( $MODIS_{mean}$ ) were used within the  
 1023 climatological approach to model hourly FRP (see Sect. 3.5).

Land cover	$\sigma$ (hour)	$\rho_{peak}$ (MW)	$\rho_{base}$ (MW)	$h_{peak}$ (hour)	$\rho_{peak}/MODIS_{mean}$ (-)
Temperate forest	1.14 (0.55)	846 (392)	24.2 (12.7)	13.31 (4.50)	3.17
Tropical forest	0.85 (0.45)	1364 (863)	27.3 (19.6)	13.34 (2.57)	3.03
Woody savanna	0.94 (0.50)	1501 (934)	21.1 (16.8)	13.21 (2.08)	3.07
Savanna	1.09 (0.53)	1711 (899)	39.0 (25.5)	13.08 (2.58)	2.88
Shrubland	1.35 (0.63)	3079 (1552)	108.9 (56.9)	13.16 (4.46)	2.87
Grassland	1.06 (0.53)	1642 (863)	37.3 (21.1)	12.95 (4.44)	3.08
Cropland	0.95 (0.48)	1259 (705)	23.9 (16.0)	13.33 (3.22)	2.94

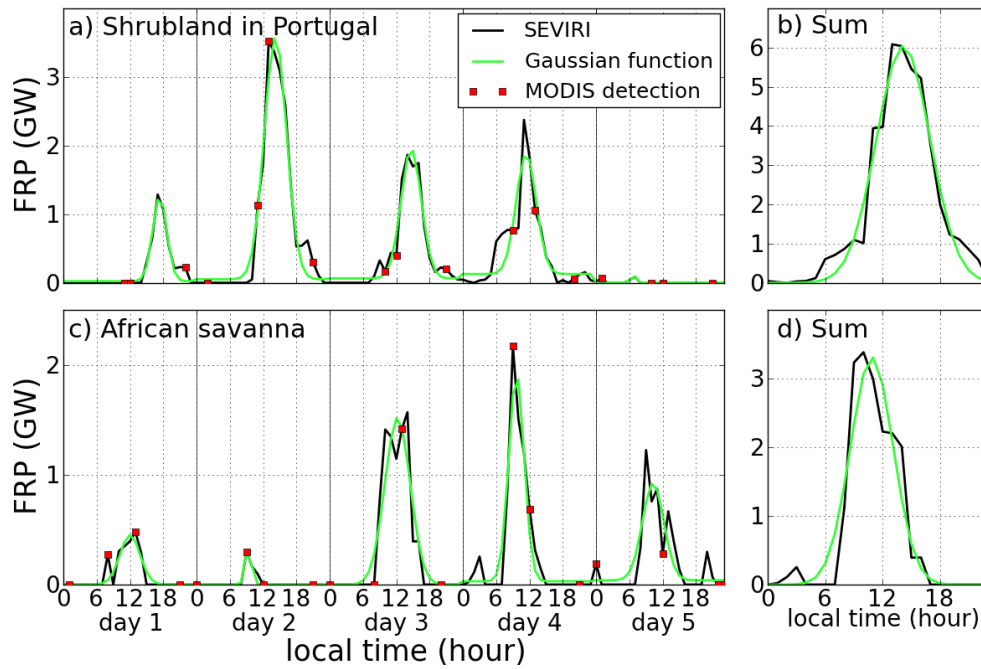
1024 Table 2. Estimated annual FRE during 2010–2012 by the two model approaches as percentage of  
 1025 SEVIRI FRE (cloud corrected).  
 1026

Land cover	SEVIRI (PJ yr <sup>-1</sup> )	Persistent (%)	Climatological (%)
Temperate forest	2.9	98	118
Tropical forest	61.3	179	98
Woody savanna	1513.2	174	93
Savanna	990.7	155	99
Shrubland	91.7	120	115
Grassland	106.5	125	108
Cropland	74.5	147	90
Total	2841.9	163	97

1027 Table 3. Pearson's r between hourly and daily FRE as observed by SEVIRI and estimated by the two  
 1028 modelling approaches. Correlation is calculated for two spatial scales, the original 0.1° resolution and  
 1029 a 1° aggregated resolution (in parentheses) to test regional model performance.  
 1030

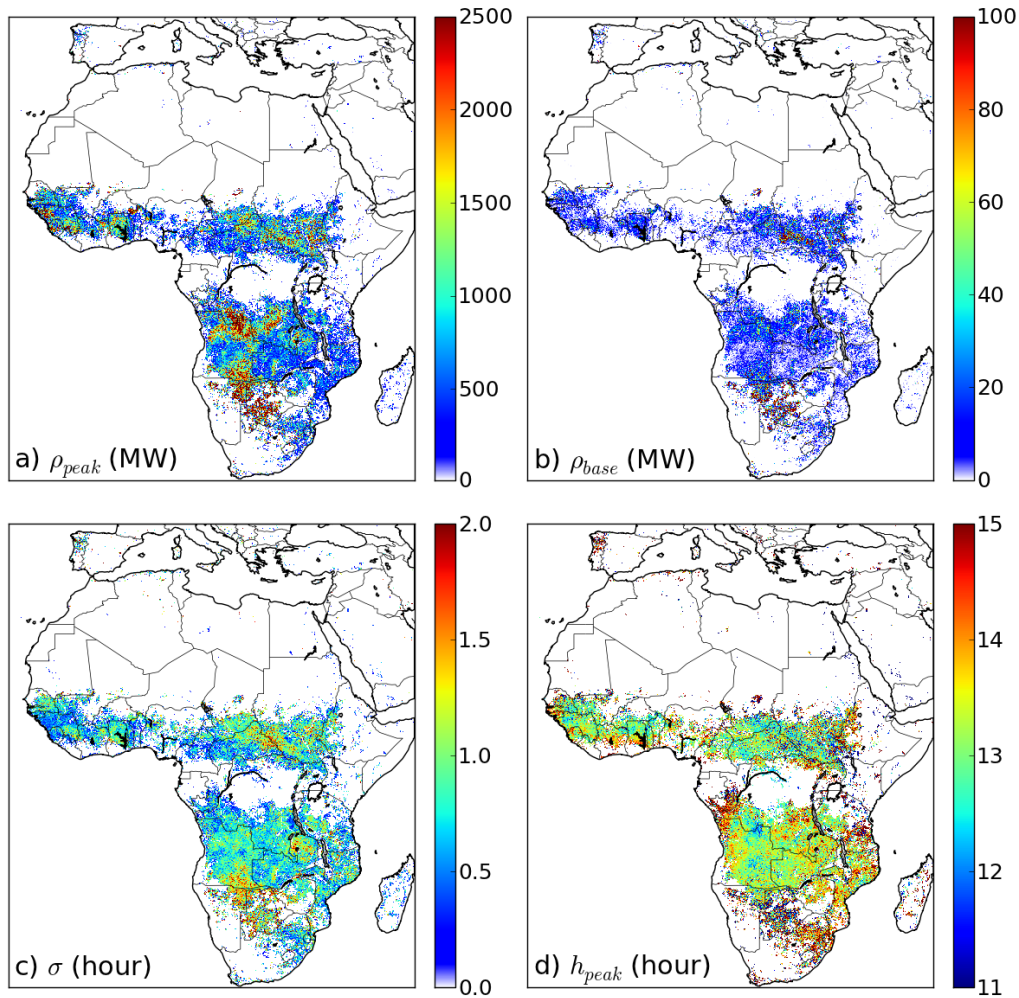
Land cover	Persistent hourly	Climatological hourly	Persistent daily	Climatological daily
Temperate forest	0.24 (0.33)	0.20 (0.32)	0.44 (0.50)	0.21 (0.39)
Tropical forest	0.13 (0.25)	0.15 (0.27)	0.32 (0.41)	0.16 (0.41)
Woody savanna	0.19 (0.44)	0.20 (0.52)	0.48 (0.80)	0.25 (0.79)
Savanna	0.25 (0.45)	0.25 (0.51)	0.54 (0.78)	0.30 (0.76)
Shrubland	0.35 (0.47)	0.32 (0.47)	0.61 (0.63)	0.37 (0.60)
Grassland	0.22 (0.32)	0.20 (0.35)	0.46 (0.55)	0.22 (0.52)
Cropland	0.19 (0.32)	0.17 (0.36)	0.42 (0.61)	0.18 (0.60)
Total	0.22 (0.43)	0.22 (0.50)	0.50 (0.76)	0.27 (0.75)

1031



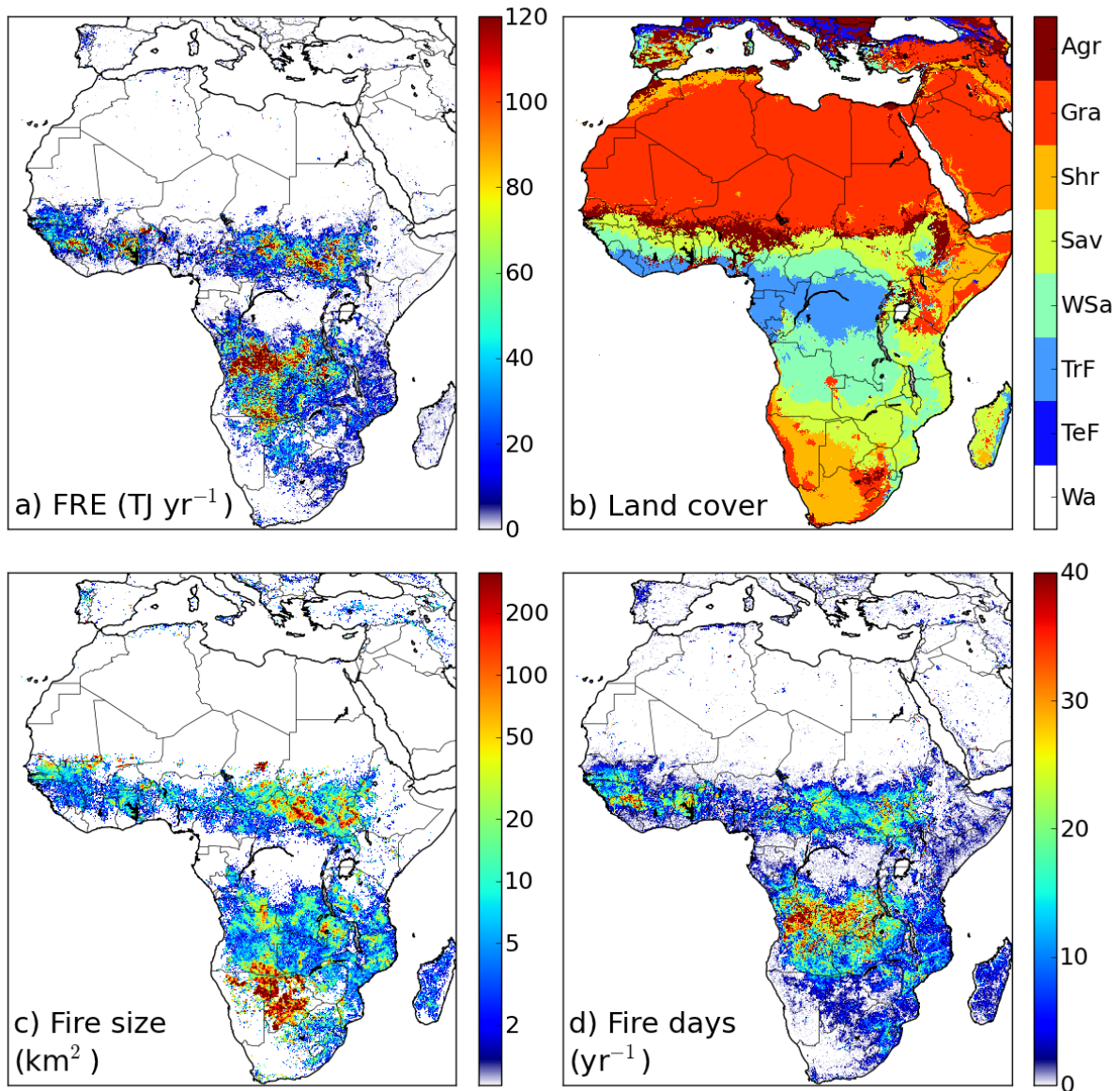
1032  
 1033  
 1034  
 1035  
 1036  
 1037  
 1038

Figure 1. Hourly-mean FRP time-series derived from SEVIRI data, the same data but only sampled at MODIS detection opportunities, and an optimally fitted Gaussian function fitted to the full SEVIRI FRP time-series. These two examples are for a 0.1° shrubland grid cell in Portugal (a, b) and a 0.1° savanna grid cell in Africa (c, d). (a, c) represent the hourly time-series and (b, d) the aggregated fire diurnal cycle over the 5 study days. Time is indicated as local time.

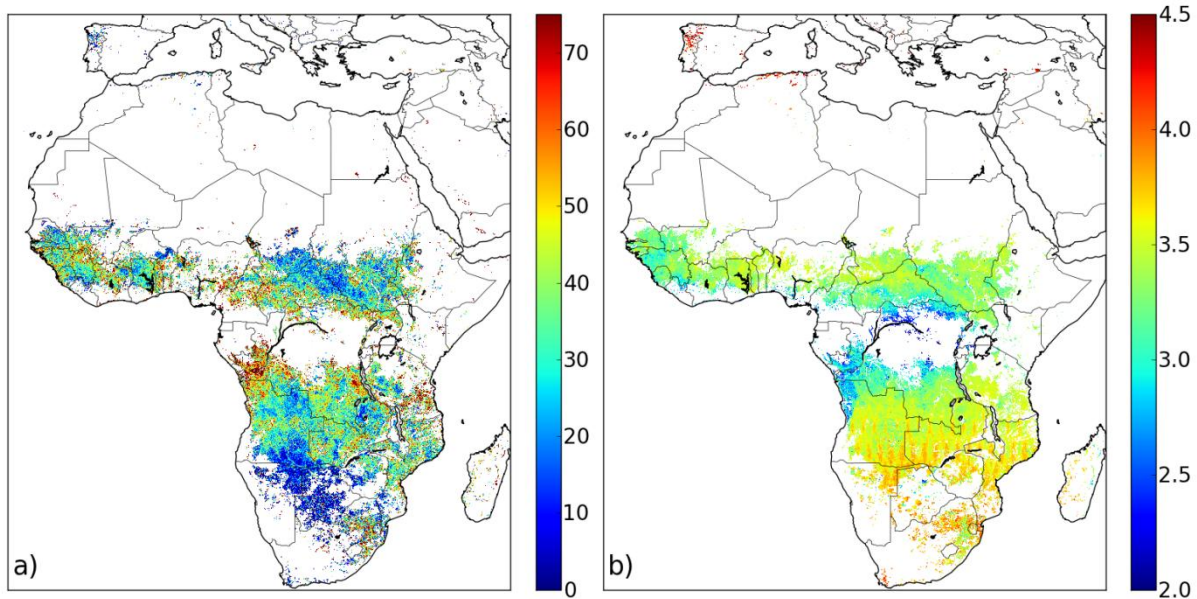


1039  
 1040  
 1041  
 1042  
 1043  
 1044  
 1045  
 1046

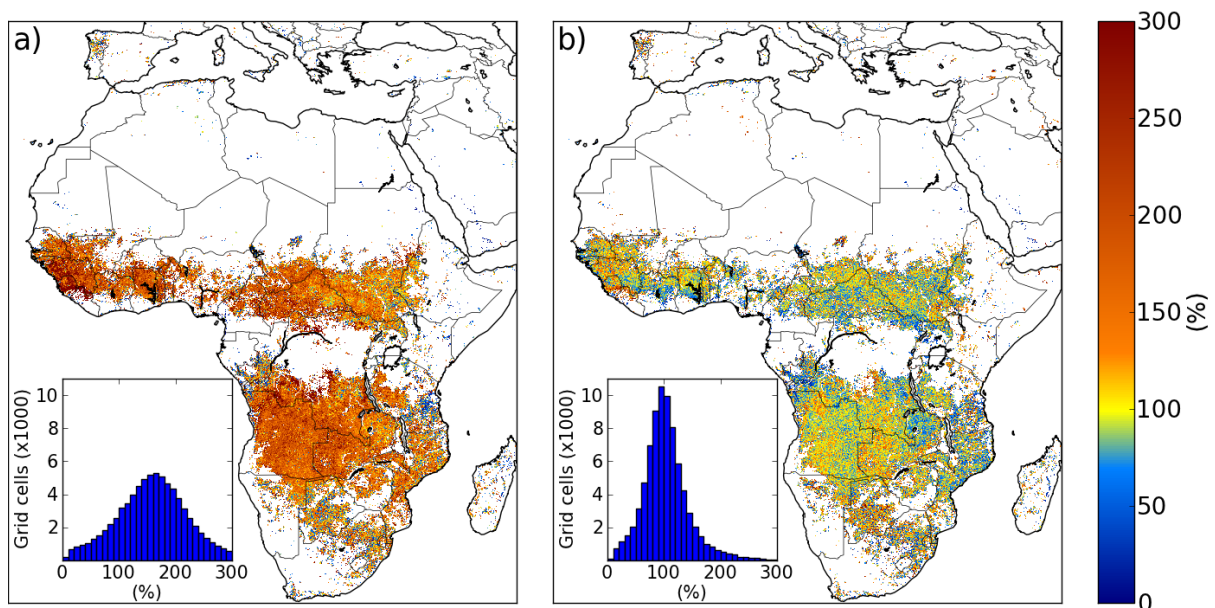
Figure 2. Weighted mean values of parameters of the optimally fitted Gaussian model for each  $0.1^\circ$  grid cell, including all cloud free days during the study period. (a) Peak daytime FRP  $\rho_{peak}$ , (b) night time FRP  $\rho_{base}$ , (c) SD of the FRE distribution over the day  $\sigma$  (related to the fire duration over the day, or width of the diurnal cycle), and (d) hour of peak fire activity  $h_{peak}$  (local time). Grid cells with emitted energy below 5 MJ over the study period (approximately the FRE emitted during one small fire event) were excluded from the figure to facilitate interpretation.



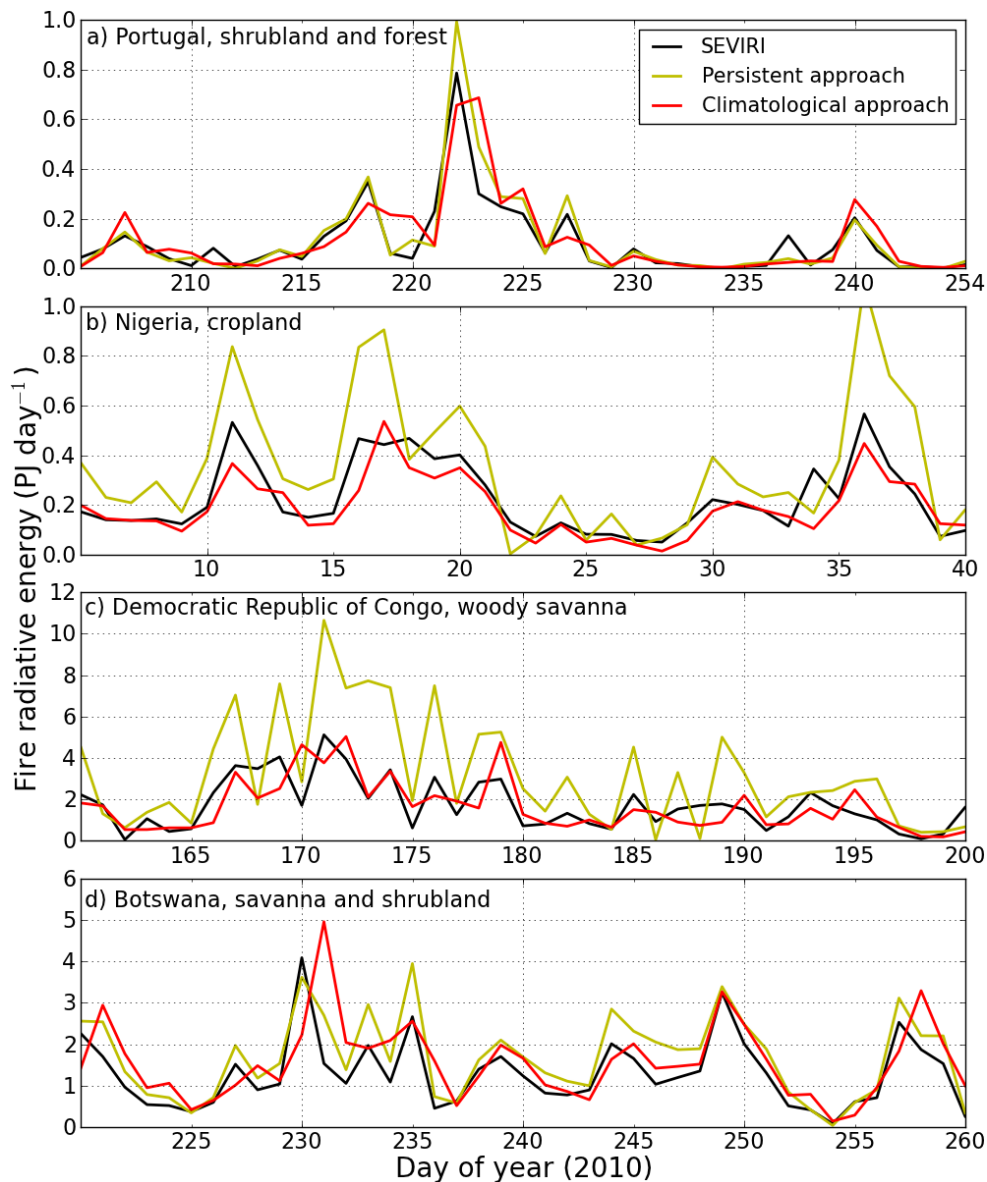
1047  
 1048 Figure 3. Characteristics of the fire regime and fuel types based on 2010 – 2012 data. (a) Mean  
 1049 annual FRE per 0.1° grid cell, (b) dominant land cover type, (c) fire size (i.e., weighted mean burned  
 1050 area per fire event) and (d) mean annual number of days with fire activity per grid cell over the study  
 1051 period. Abbreviations of land cover classes: water (Wa), temperate forest (TeF), tropical forest (TrF),  
 1052 woody savanna (WSa), savanna (Sav), shrubland (Shr), grassland (Gra) and agriculture (Agr).  
 1053



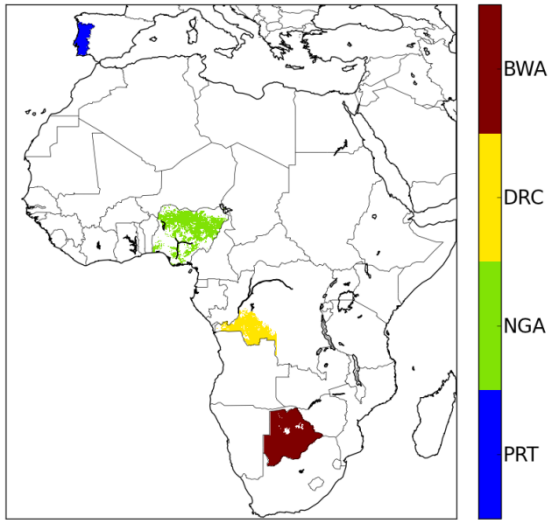
1054  
 1055 Figure 4. Detection of fire activity at MODIS detection opportunities. (a) Percentage of FIRE emitted  
 1056 on days that the SEVIRI instrument did not observe active fires at MODIS overpasses. (b) Number of  
 1057 MODIS detection opportunities per day during the burning season (mean over the study period,  
 1058 weighted for monthly FRP).  
 1059



1060  
 1061 Figure 5. Total fire radiative energy (FRE) estimated via the two modelling approaches using SEVIRI  
 1062 observations taken at only the MODIS detection opportunities, expressed as fraction of the total FRE  
 1063 calculated using the entire set of hourly mean, 0.1° SEVIRI FRP observations (cloud cover corrected).  
 1064 (a) Persistent approach, and (b) climatological approach. Distribution of the grid cell values is shown  
 1065 in the lower left corners.  
 1066



1067  
 1068 Figure 6. Daily FRE for four study regions (areas of 85000 to 567000 km<sup>2</sup>) derived from the complete  
 1069 SEVIRI dataset (cloud cover corrected) and estimated by the two modelling approaches developed  
 1070 here. (a) Daily FRE for Portugal, mostly including shrublands and temperate forests, (b) fires in  
 1071 Nigeria burning in croplands, (c) woody savannas in DRC, and (d) shrublands and savannas in  
 1072 Botswana. Study regions are shown in Fig. 7, and land cover was determined using the dominant land  
 1073 cover classes (Sect. 2.3; Fig. 3b).



1074  
1075  
1076  
1077  
1078

Figure 7. Study regions used in Fig. 6. Abbreviations refer to: Botswana (BWA), the Democratic Republic of Congo (DRC), Nigeria (NGA) and Portugal (PRT).